#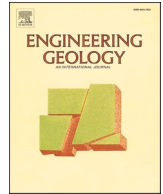 Identification of key thermal couplings affecting the bentonite behaviour in a deep geological nuclear waste repository

(article starts on next page)

Identification of key thermal couplings affecting the bentonite behaviour in a deep geological nuclear waste repository

Abhishek Gupta [a,*], Ayman A. Abed [b], Wojciech T. Solowski [a]

[a] *Department of Civil Engineering, Aalto University, Espoo 02150, Finland*
[b] *Department of Architecture and Civil Engineering, Chalmers University of Technology, Gothenburg SE-412 96, Sweden*

ARTICLE INFO

ABSTRACT

Deep geological nuclear waste repositories use the multi-layer Engineered Barrier System (EBS) to isolate nuclear waste from the environment. The key component of the barrier is densely compacted bentonite, closely resembling claystone. Therefore, to ensure safety, we need a numerical model for the bentonite and the barrier that predicts EBS behaviour during transient thermal, hydraulic, mechanical and chemical conditions. The paper identifies key mechanisms and processes affecting the bentonite in the barrier due to temperature changes (thermal couplings) based on advanced fully-coupled Finite Element Method simulations. The paper investigates 1) non-isothermal infiltration experiment on FEBEX bentonite (Villar and Gomez-Espina, 2009) and, 2) Centro de Investigaciones Energeticas Medioambientales y Tecnologicas (Ciemat) test (Martin et al., 2006), presenting 10 simulation configurations that are set up by inactivating one thermal coupling/variable at a time. The difference between these simulations and the baseline model results, examined in terms of the net mean stress (swelling pressure), suction and fluid flow, give insights into the significance of investigated coupling. Results suggest that thermal couplings related to vapour density, viscosity, water retention curve, and molecular diffusivity are among the most influential. The study additionally highlights the importance of water transport as liquid and gas, and water evaporation and condensation.

Symbols

D_{atm}	molecular diffusivity of water vapour in air, $L^2 T^{-1}$	$\mathbf{K_i}$	hydraulic conductivity (where i = liquid or gas), LT^{-1}
D_{vT}	molecular diffusivity due to temperature, $ML^{-1}T^{-1}\Theta^{-1}$	$\mathbf{K^l_{sat}}$	liquid phase saturated hydraulic conductivity, LT^{-1}
D_{vw}	molecular diffusivity due to moisture, $ML^{-2}T^{-1}$	L	latent heat of water vaporization $L^2 T^{-2}$
$\mathbf{D^e}$	Elastic stiffness matrix	M	slope of critical state line
E	Young's modulus, $ML^{-1}T^{-2}$	M_a	molar mass of dry air, $Mmol^{-1}$
F	yield function	M_w	molar mass of water vapour, $Mmol^{-1}$
f_{Tv}	thermal enhancement factor	$\mathbf{m}$	auxiliary vector, {1,1,1,0,0,0}
g	earth gravity acceleration, LT^{-2}	n	soil porosity
$\boldsymbol{b}$	Body force vector, $ML^{-2}T^{-2}$	p_0	isotropic pre-consolidation pressure, $ML^{-1}T^{-2}$
g_α, g_n, g_m	van Genuchten curve fitting parameters	p_0^*	pre-consolidation pressure at suction (s) = 0, $ML^{-1}T^{-2}$
H	Henry's volumetric coefficient of solubility	p	net mean pressure, $ML^{-1}T^{-2}$
h_g	gas pressure head, L	p_s	BBM term that relates to suction induced strength increase, $ML^{-1}T^{-2}$
h_w	water pressure head, L	p^c_{ref}	reference pressure in BBM, $ML^{-1}T^{-2}$
$\mathbf{j^i_k}$	non-advective flux of component k, $ML^{-2}T^{-1}$	Q^i_k	sink/source term of component k, $ML^{-3}T^{-1}$
k	parameter that controls the term p_s in Barcelona basic model (BBM)	$\boldsymbol{q}$	Darcy velocity, LT^{-1}
		q	deviatoric stress, $ML^{-1}T^{-2}$
		$\boldsymbol{q^T}$	conductive heat flux, MT^{-3}

$\mathbf{q_h}$	total heat flux, MT^{-3}
R	universal gas constant, $ML^2\,T^{-1}\,\Theta^{-1}\,mol^{-1}$
RH	relative humidity
r	BBM parameter related to maximum stiffness of soil
S^g	degree of gas saturation
S^l	degree of liquid saturation
S^l_{res}	degree of liquid saturation at residual state
S^l_{sat}	degree of liquid saturation at full saturation
s	suction, $ML^{-1}\,T^{-2}$
T	absolute temperature, Θ
T_0	Reference absolute temperature, Θ
T_{ref}	273.16 K temperature, Θ
t	time, T
$\boldsymbol{\nu}^{\mathbf{i}}$	Velocity vector of phase i, LT^{-1}
v_v	mass flow factor
α_o, α_2	elastic thermal strain parameters
α_1, α_3	parameters control the thermal effects on pre-consolidation pressure
α_κ	parameter control κ value of BBM
$\alpha_{\kappa s1}, \alpha_{\kappa s2}$	parameters control κ_s value
β	BBM parameter that controls the suction related change in soil stiffness, $M^{-1}LT^2$
β_{sT}	coefficients of thermal expansion in solids, Θ^{-1}
β_{wT}	coefficients of thermal expansion in water, Θ^{-1}
β_{wp}	coefficient of water compressibility, $M^{-1}LT^2$
$\dot{\boldsymbol{\varepsilon}}_{\mathbf{e}}$	total elastic strain rate vector
$\dot{\varepsilon}_e^s$	elastic strain rates due to suction
$\dot{\boldsymbol{\varepsilon}}_{\mathbf{e}}^{\boldsymbol{\sigma}}$	elastic strain rates due to net stress vector
$\dot{\varepsilon}_e^T$	elastic strain rates due to temperature
ε_v	infinitesimal volumetric strain
γ^T	material constant that relates to change in saturated pre-consolidation pressure
Φ_h	soil heat capacity, $ML^{-1}\,T^{-2}$
ϕ^i	volume fraction of phase i
κ, κ_o	BBM elastic parameter and is its reference value, respectively
κ_s, κ_{so}	suction related BBM elastic parameter and its reference value, respectively
λ	BBM parameter related to soil stiffness
λ_T	thermal conductivity, $MLT^{-3}\Theta^{-1}$
ν	Poisson's ratio
μ_l	liquid phase dynamic viscosity, $ML^{-1}\,T^{-1}$
ρ_a	dry air density, ML^{-3}
ρ^b	bulk density, ML^{-3}
ρ^i	density of phase i, ML^{-3}
ρ_w^l	water density in liquid phase, ML^{-3}
ρ_w^g	vapour density, ML^{-3}
ρ_{w0}^g	saturated vapour density, ML^{-3}
ρ^T	thermal BBM parameter
$\boldsymbol{\sigma}$	net stress, $ML^{-1}\,T^{-2}$
$\boldsymbol{\sigma}^{\mathbf{tot}}$	total stress, $ML^{-1}\,T^{-2}$
σ^t, σ_0^t	surface tension of water and its reference value, MT^{-2}
σ_y	vertical net stress, $ML^{-1}\,T^{-2}$
σ_r	radial net stress, $ML^{-1}\,T^{-2}$
τ	tortuosity
ω_k^i	mass fraction of component k in phase i
ξ_n^T	curve fitting parameter, Θ^{-1}
ξ_w^T	curve fitting parameter, Θ^{-1}
ψ	matric suction head, L
$\dot{}$	derivation with respect to time
∂	partial differentiation operator
∇	gradient operator
div	divergence operator

Subscripts

a	dry air component
g	gas phase
k	component (k = a, air; w, water; s, solid)
s	solid component
T	temperature
v	water vapour
w	water component

Superscripts

e	elastic
g	gas phase
i	phase (i = s, solid; l, liquid; g, gas)
l	liquid phase
s	solid phase
tot	total
v	volumetric

Abbreviation

EBS	engineered Barrier System
THMC	thermo-hydro-mechanical and chemical
BBM	Barcelona basic model
FEM	finite element method

1. Introduction

Deep geological deposition of nuclear energy waste is one of the safest options to ensure negligible exposure of the waste to the environment (OECD-NEA, 2003; Ye et al., 2009). The deep geological depository consists of several barriers that prevent the transport of radionuclides: a canister holding radionuclides, a barrier expansive soil layer, a concrete/steel liner, and a host rock. In such Engineered Barrier Systems (EBS), unsaturated bentonite is typically employed in the barrier to prevent the transport of radioactive material (Hoffmann et al., 2007; Sellin and Leupin, 2014). Upon saturation, highly compacted bentonite develops swelling pressure and becomes claystone-like rock with a very low permeability. This leads to crack-sealing capability, enabling the barrier to tolerate multi-physical actions, such as heat from radioactive waste and gas (such as H_2) penetration from possible anaerobic corrosion (Wilson et al., 2011). To ensure safety, barrier design requires the barrier to isolate the waste from environment for at least thousands of years. As experiments are limited to a much shorter time periods, safe long-term bentonite barrier design requires efficient predictive computational modelling of the complex coupled behaviour. The sections below provide a general introduction to modelling approaches (1.1), the purpose of examining critical couplings in THM models and present studies (1.2) and the novelty, aim and methodology of the paper (1.3).

1.1. Advancements in modelling and relevance of traditional approaches

Several Finite Element (FEM) or Finite Volume Method computer codes can model coupled behaviours in bentonite ranging from simple thermal-hydraulic considerations to codes that can simultaneously consider more advanced thermal-hydraulic-mechanical or chemical couplings (for example: Collin et al., 2002; Gens et al., 2010; Abed and Sołowski, 2017; Zheng et al., 2017; Zhou et al., 2021). Recent research has enhanced understanding of the mechanical behaviour of expansive clay as well as the gas transport processes by including damage or fracture modelling and micro-macro pore structuration (Alonso et al., 1999; Arson and Gatmiri, 2008; Guo and Fall, 2018; Villar et al., 2020; Navarro et al., 2022). The dual porosity models also address the coupling between micro-macro pores when evaluating water retention

and suction behaviour, either through a leakage term (Sánchez et al., 2016) or by fully incorporating two void levels into the framework (Mašín, 2013; De la Morena et al., 2021). Furthermore, recent studies by Navarro et al. (2020) and Abed and Sołowski (2021) explore the use of a third pore level. The use of a constitutive model that takes the evolution of porosity of bentonite into account could increase the accuracy of the mechanical response of the model, but also increase the number of material parameters needed, and the uncertainty related to their values. As the paper focuses on processes related to temperature, we think that the use of extensively validated Barcelona Basic Model (Alonso et al., 1990), the most established constitutive model for bentonite with very well-known responses, shortcomings and well-established extensions related to temperature (Gens, 1995; Laloui and Cekerevac, 2003; Sánchez et al., 2012) is justified.

Furthermore, reactive modelling is an additional area of focus that concerns radionuclide transport, salt reactive mechanically coupled behaviour or higher temperature ranges (above 100 °C) (Liu et al., 2013; Zheng et al., 2017; Tran et al., 2018; Medved and Černý, 2019; Scelsi et al., 2021). However, addressing changes in soil composition or the dynamic thermal state of the soil matrix may lead to more numerical uncertainties.

To summarise, although modelling practices are evolving, a classical approach that accounts for two-phase flow and adopts a (single) porosity elastoplastic model within the range of 100 °C is still widely employed for deep geological repository simulations (Rutqvist et al., 2001; Schäfers et al., 2020; Gens et al., 2021). The used framework stands relevant primarily because of their relative simplicity, lower number of input parameters and widely available data for model calibration. Additionally, in practice, most repository design concepts so far include a design criterion of 100° C as the maximum temperature allowed (Johnson et al., 1994; SKB, 1999).

1.2. Previous studies on critical couplings in THM modelling of bentonite

Though extensively in use, the reliability of the THM models depends on their capability in replicating multiple physical processes in bentonite or claystone in a deep geological repository. For example, due to the heat generated by the waste, water evaporates near the heating side (nuclear waste source) and progresses towards the outer regions of an unsaturated bentonite layer where it condensates. Simultaneously, the hydraulic pressure difference causes liquid water to flow from the host rock towards the heating source. Hence, bentonite hydrates at the outer surface, with water gradually moving inwards to the nuclear waste source (Gens et al., 2021), until a balance between competing water transport mechanisms is found.

Modelling such intricate physical processes, therefore, requires several constitutive relationships. Among others, Nguyen-tuan et al. (2017) and Kim et al. (2019) performed LSA (local sensitivity analysis) and GSA (global sensitivity analysis) to explore parameter sensitivity in THM modelling. Nguyen-tuan et al. (2017) investigated a total of 20 parameters associated with different constitutive relationships such as Darcy's law, Fick's law, Fourier's law, retention curve, and extended Barcelona Basic Model (BBM) soil model (Alonso et al., 1990; Hoffmann et al., 2007; Sánchez et al., 2012). The findings highlight the significance of some commonly noted factors in other similar works (Ballarini et al., 2017; Kim et al., 2019), such as thermal conductivity, water retention curve, and permeability. Additionally, the study suggests that the model is sensitive to factors related to vapour diffusion and BBM parameters such as $\alpha_{\kappa s1}$, α_{κ}, $\alpha_{\kappa s2}$ and α_0 (see, section 2.2.1 for BBM model details). The advantage of such an approach is the ease of evaluating several parameters. However, since these studies mainly focus on quantifying parameter sensitivity, they lack insight into the couplings influence on the physical processes occurring in a geological repository.

In comparison, a more fundamental approach is investigating the interplays of different phenomena influenced by the examining parameters. Experimentally, it is possible to analyse specific coupled physics in a controlled environment (Börgesson et al., 2001; Villar and Lloret, 2004). These methods are relevant in understanding the material behaviour under varying conditions and further for the back-analysis of numerical models. However, experimentally investigating the interactions is challenging when involving all the coupled repository phenomena in a single test setup. For instance, Villar and Lloret (2004) performed tests of saturation of bentonite under a vertical load. Since the experiment is under a thermostatic setup, the different temperature profiles at every test repetition allow for only examining the influence of the temperature and loading on swelling strains.

Meanwhile, numerical models enable analysing the effect of a specific constitutive relation simultaneously on several different coupled material behaviours of bentonite under THM conditions. Moreover, testing the influence of various factors is easier to implement while offering quick and crucial insight into the sensitivity of coupled relations that enables a physical aspect in a model. Gens et al. (1998) investigated the influence of the absence of vapour diffusion, retention curve with different air entry values and no thermal loading on an experimentally validated simulation. A comprehensive exploration details the development of dominating physical mechanisms in each scenario that leads to a change in saturation, volume, pressures and stresses.

In a similar approach, an early study by Wang et al. (2011) critically analysed the influence of different vapour/gas transport mechanisms. The mechanisms are as follows: a) Richards approach with diffusive vapour flow and no bulk gas flow, and b) two-phase flow. The finding suggests that ignoring two-phase flow at lower intrinsic permeabilities shows higher sensitivity.

There are only a few more comparable studies, most of which consider analysing critical phenomena and studying the interaction as a secondary aim. Additionally, similar to the works mentioned earlier, such research usually investigates general or more fundamental relations and ignores the influence of several physically coupled subprocess. For example, vapour diffusion depends on sub-process like varying vapour density or diffusivity with temperature. Many studies (ex. Zheng et al., 2010; Ballarini et al., 2017) indulging in this approach aims at achieving a good match between their model and experiment by controlling the response of these relations through sensitivity and back analyses of associated parameters. Ballarini et al. (2017) reported thermal conductivity, water retention curve, permeability, and relative permeability as sensitive parameters in their THM modelling. Similarly, Lee et al. (2014) found thermal conductivity and viscosity sensitive to their thermal-hydraulic model. In general, such studies broadly cover sensitivity analysis for relatively fewer parameters and often fell short in detailed insights.

Apart from these, code comparison studies (Schäfers et al., 2020; Gens et al., 2021) with an aim to assess the capabilities of different numerical formulations in simulating the observed THM behaviour also occasionally hint at the influence of certain physical couplings by reporting discrepancies in the results, but with little insights. For instance, the consequence of constant hydraulic conductivity, porosity variation with suction or constant viscosity.

In recent years, the only relevant study we found is by Dupray et al. (2013). The study identifies the importance of some physical and coupled processes, such as vapour creation and diffusion in the resaturation of soil through condensation, the influence of hydraulic and thermal-related couplings on mechanical response etc. Yet, the study examines only six scenarios out of many possible numerically feasible physical relations. For example, several thermal couplings representing small physical features like variation in vapour diffusion, saturated vapour density or relative humidity and suction equilibrium condition govern the process of vapour production and flow are missed. However, Dupray et al. (2013), similar to Gens et al. (1998), examined only a case of no vapour diffusion, limiting its usefulness. Furthermore, the study lacks few commonly applied features like a thermally extended Barcelona Basic model (BBM) and thermally coupled retention curve (Olivella and Gens, 2000; Rutqvist et al., 2011; Abed and Sołowski, 2017).

Beyond the mentioned works, that examine the influence of couplings, specifically, relations that enable various thermally coupled physical sub-features in a bentonite material behaviour are close to none.

1.3. Novelty and study approach

The current work offers an in-depth assessment of different thermal couplings enabling various physical thermal responses of bentonite. The novelty of this work lies in its focus on the developments and interactions of different phenomena in bentonite under THM conditions, influenced by several thermal couplings by using simulations of experiments. This aligns with an approach taken by Gens et al. (1998) but examines factors relating to less explored thermal processes instead of well-researched fundamental couplings that represent a broader phenomenon in previous literature such as vapour consideration, permeability variation or thermal conductivity. The study analyses relations that are overlooked in previous works with the same methodology, among others, this includes temperature-dependent relations like retention curve, saturated vapour density, relative humidity and suction equilibrium condition and BBM. Further, the objective is to identify key coupling relations important for bentonite behaviour in a nuclear repository like THM conditions. Such an approach avoids the sensitivity measuring methods requiring multiple simulations like LSA/GSA, Monte Carlo simulations or Taguchi's experimental design method (Narkuniene et al., 2015; Nguyen-tuan et al., 2017; Lafifi et al., 2019). This leverages data readability, detection, and comparison of behavioural changes.

The obtained results help recognize important physical features that require closer attention while defining the associated numerical relationship in modelling bentonite or claystone behaviour under THM repository conditions. Additionally, the results can aid in optimizing approaches leading to more efficient simulations. Since traditional THM models for nuclear repository simulation mostly involve a similar level of complexity and coupling producing comparable results (Schäfers et al., 2020; Gens et al., 2021), unlike parameter sensitivity, the research can also aid these studies that may use different numerical relations but for the same physical aspects of bentonite. Moreover, the outcomes of this research can be extended to soil and rock groups with high montmorillonite content, such as boom clay, claystone, or mudstone, which share analogous characteristics to bentonite. Modelling their THM characteristics typically follows similar considerations (Alonso et al., 1999; Rutqvist et al., 2014). Given that these materials serve as potential geological host formations for nuclear repositories (Ortiz et al., 2002; Xu et al., 2013; Armand et al., 2017), the findings of this study are highly relevant. Moreover, identifying critical physical features governing material swelling, water content, and transfer can facilitate research in analysing nuclear repository structural integrity and potential geological hazards related to gas or radionuclide transport. Lastly, an understanding of dominating physical process can assist in the critical analysis of deep geological repository models.

Note, the study primarily examines simulations of experiments within the temperature range below 100 °C, which aligns with the common design and numerical considerations for nuclear repository simulations as mentioned in section 1.1. Consequently, the insights provided in this paper are confined to this temperature range. It is worth noting that there is limited research addressing the THM behaviour of bentonite at higher temperatures. In such a scenario, it is crucial to analyse factors such as thermal conductivity, the long-term effects of vapour exposure on bentonite, and potential mineralogical changes (Önal and Sar, 2007; Wersin et al., 2007). However, these aspects exceed the scope of the current work.

Two cases that enable THM-like repository conditions in bentonite are under consideration for the analysis, using a finite element (FE) program code Thebes (Abed and Sołowski, 2017). The experimental tests are: 1) non-isothermal infiltration experiment on FEBEX bentonite (Villar and Gomez-Espina, 2009) and, 2) Centro de Investigaciones Energeticas Medioambientales y Tecnologicas (Ciemat) Mock-up test (Martin et al., 2006). These experiments differ in test scale, boundary conditions, and soil properties, and several studies used them as benchmark cases (Chen et al., 2009; Sánchez et al., 2016; Potts et al., 2021). Additionally, Abed and Sołowski (2017, 2020) provide extensive validation of the code Thebes against the experiments. Therefore, they provide sufficient reliability and variability to perform a critical analysis of the influence of thermal couplings. Ten trial simulation configurations are set up for examination by deactivating thermal couplings one at a time. Finally, the paper presents an assessment of coupling effects on hydration and swelling characteristics of bentonite by comparing the net mean stress (swelling pressure in repository conditions), suction, and fluid flow results of the trial simulations against the baseline simulations by Abed and Sołowski (2017, 2020).

2. Influence of temperature in FEM code Thebes

Thebes is a finite element code designed to model the coupled THMC behaviour in unsaturated clays like bentonite (Abed and Sołowski, 2017, 2020). The thermal coupling equations investigated in this paper are part of the Thebes Finite Element framework. Although the coupling equations are specific to the Thebes code, the research outcomes are still helpful to other THM models replicating the same physical aspects of bentonite behaviour.

The present section helps to understand the thermal couplings under consideration and the trial test configurations. For this, the section first briefs on Thebes general framework (section 2.1) and later explains the physical aspect of individual thermal coupling equations (section 2.2) and the final test configurations (section 2.3).

2.1. Thebes overview

In Thebes, the soil model encompasses three components (soil solid particles, water, and dry air), in three phases (see, Fig. 1): a) soil particles in a solid phase, b) liquid water + dissolved dry air in a liquid phase, c) dry air + water vapour in a gas phase. The latest version of the code also includes an extra component as salts in the solid phase (Abed and Sołowski, 2020). However, it is out of the scope of this work.

The THM framework in Thebes utilises conservation equations, namely: a) mass balance of the components, b) heat conservation and, c) balance of mechanical forces. Each has been detailed, separately in this section.

As the presented framework can be easily applied for other THM coupled problems, this section of the paper adopts the universally accepted sign convention of continuum mechanics, where negative values are assigned to compressive stress and strain.

2.1.1. Mass conservation of components

Mass conservation follows the compositional method in Thebes (Panday and Corapcioglu, 1989). A general form for the mass balance of any component is given by eq. (1). It includes a mass storage term and mass flow terms: advection and non-advection (e.g., diffusion).

$$\underbrace{\frac{\partial(\phi^i \rho^i \omega_k^i)}{\partial t}}_{storage} + \underbrace{div(\phi^i \rho^i \omega_k^i \boldsymbol{v}^i)}_{advection} + \underbrace{div(\boldsymbol{j}_k^i)}_{non\text{-}advection} = \underbrace{Q_k^i}_{source}$$

where t is time and for the ith phase: ϕ^i is the volume fraction, ρ^i is the density, ω_k^i is the mass fraction of component k, $\boldsymbol{v}^i$ is the velocity vector, $\boldsymbol{j}_k^i$ is the non-advective flux vector of component k and Q_k^i is the source term of component k. Here, in the absence of any external sink/source, the summation of the component k source term in all the phases becomes zero i.e., $\sum Q_k^i = 0$. Further, to ensure mass balance, the sum of the non-
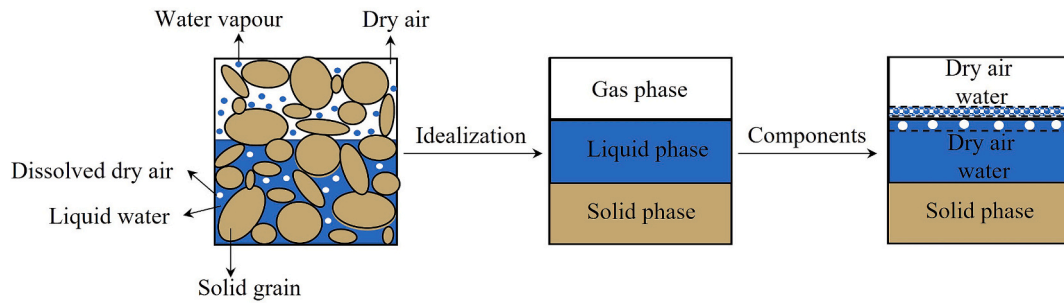
Fig. 1. Soil model in Thebes with different components and phases labelled (Abed and Sołowski, 2017).

advective terms follows a constraint as, $\sum_{k}^{m}\mathbf{j_k^i} = 0$ (k components and m phases).

Based on eq. (1), the mass balance of solids leads to an expression (eq. 2), that shows the rate of change in porosity depends on the rate of volumetric strain due to mechanical load as well as the volume change of solid particles due to change in temperature. The expression however does not account for soil particles compressibility. Its derivation can be found in Abed and Sołowski (2017).

$$\frac{\partial n}{\partial t} = (1 - n)\left(\frac{\partial \varepsilon_v}{\partial t} - \beta_{st}\frac{\partial T}{\partial t}\right) \tag{2}$$

where n is the current soil porosity, ε_v is the volumetric strain and β_{st} is the coefficient for volumetric thermal expansion of solids.

Further, the mass balance of water component [kg/m³.s] is expressed as follows:

Moreover, Thebes uses Philip and De (1957) expression for the vapour diffusion ($\mathbf{j_w^g}$), eq. (5).

$$\mathbf{j_w^g} = -D_{vw}\nabla h_w + D_{vw}\nabla h_g - D_{vt}\nabla T \tag{5}$$

where the terms with diffusion coefficient (D_{vw}) relate to flow due to suction variation, whereas the term with (D_{vt}) relates to flow due to temperature variation.

To evaluate the rate of degree of saturation $\partial S^l/\partial t$, Thebes implements a thermal version of van Genuchten's expression relating saturation (S^l) to suction (ψ), (van Genuchten, 1980; Jacinto et al., 2009):

$$S^l = \left(S_{sat}^l - S_{res}^l\right)\left[1 + (g_a|\psi|)^{g_n}\right]^{g_m} + S_{res}^l \tag{6}$$

where S_{sat}^l, S_{res}^l represent the degree of saturation at full and residual state, respectively. g_a, g_n and g_m are temperature dependent curve fitting parameters (see, section 2.2.2. for more details).

$$\left[n(\rho_w^l - \rho_w^g)\frac{\partial S^l}{\partial T} - (1-n)(S^l\rho_w^l + S^g\rho_w^g)\beta_{sT} - nS^l\beta_{wT}\rho_w^l + nS^g\frac{\rho_w^g}{T^2}\left(4974 + g\frac{M_w\psi}{R}\right)\right]\frac{\partial T}{\partial t}$$

$$+\left[nS^l\beta_{wp}g\rho_w^{l2} + nS^g\frac{\rho_w^g gM_w}{RT} - n(\rho_w^l - \rho_w^g)\frac{\partial S^l}{\partial\psi}\right]\frac{\partial h_w}{\partial t} + \left[n(\rho_w^l - \rho_w^g)\frac{\partial S^l}{\partial\psi} - nS^g\frac{\rho_w^g gM_w}{RT}\right]\frac{\partial h_g}{\partial t} \tag{3}$$

$$+(S^l\rho_w^l + S^g\rho_w^g)\frac{\partial\varepsilon_v}{\partial t} + div(\rho_w^l q^l) + div(\rho_w^g q^g) + div(j_w^g) = 0$$

where g is gravity acceleration, ρ_w^l is the water density in a liquid phase, ρ_w^g is the vapour density in a gas phase. S^l and S^g are the degree of saturation for liquid and gas, respectively. β_{sT} and β_{wT} are the coefficients of volumetric thermal expansion in solids and water respectively. β_{wp} is the coefficient of water compressibility, T is the temperature, M_w is the molar mass of vapour and R is the universal gas constant. $\mathbf{q^l}$ and $\mathbf{q^g}$ are the water and vapour fluxes respectively. h_w is the water pressure head and h_g is gas pressure head that is represented by its equivalent to water pressure. ψ is the matric suction head $(h_g - h_w)$ and $\mathbf{j_w^g}$ represents vapour diffusion, while the numeric value (4974) in the above expression is the result of considering empirical relation between temperature and saturated vapour density, see also eq. (27). Please refer to eq. (A.1) for the mass conservation of air component.

In the above eq. (3), for fluid fluxes (q), Thebes follows Darcy's law (Darcy, 1856). A general form of the expression for i^{th} phase (gas or liquid phase) in the direction of gravity, is given in eq. (4).

$$\mathbf{q^i} = -\mathbf{K_i}\left(\nabla h_i + \frac{\rho^i}{\rho_w^l}\right) \tag{4}$$

where $\mathbf{K_i}$ is the hydraulic conductivity. Note in case of liquid phase the term ρ^i represent water density (ρ_w^l), whereas in gas phase it becomes gas density (ρ^g).

2.1.2. Conservation of heat

The general expression considered for the conservation of heat is:

$$\underbrace{\frac{\partial\Phi_h}{\partial t}}_{\text{heat storage}} + \underbrace{LQ_w^g}_{\substack{\text{Latent heat}\\\text{of vaporization}}} + \underbrace{div(\boldsymbol{q_h})}_{\substack{\text{heat from}\\\text{conduction/convection}}} = 0$$

where Φ_h is the soil heat capacity, L is the latent heat of vaporization, Q_w^g is the rate of vapour production and $\mathbf{q_h}$ is the heat flux from conduction and convection. Here, the rate of vapour production eq. (8) representing water mass in the gas phase is derived by using eq. (1) (Abed and Sołowski, 2017).

$$Q_w^g = -(1-n)S^g\rho_w^g\beta_{st}\frac{\partial T}{\partial t} + S^g\rho_w^g\frac{\partial\varepsilon_v}{\partial t} - n\rho_w^g\frac{\partial S^l}{\partial t} + nS^g\frac{\partial\rho_w^g}{\partial t} + \nabla.(\rho_w^g\mathbf{q^g}) + \nabla.\mathbf{j_w^g} \tag{8}$$

Addressing the formulation of storage term, eq. (9) shows the general form of heat capacity, where the symbol E_{Tk}^i represents the thermodynamic state function (Diersch and Kolditz, 2002) for the internal energy of component k in phase i.

$$\Phi_h = \phi^i\rho^i\omega_k^i E_{Tk}^i \quad \left(where, \ E_{Tk}^i = c_k^i\left(T_k^i - T_{k0}^i\right)\right) \tag{9}$$

where c_k^i is the specific heat capacity of component k in phase i. Note that the above expression assumes that the different components in the soil are in thermal equilibrium (Abed and Sołowski, 2017).

Next, eq. (10) shows the general expression for total heat flux in Thebes (Abed and Sołowski, 2017). It includes: i) the contribution by conductivity heat flux ($\mathbf{q}^T$), ii) convection of heat by liquid flow ($\mathbf{q}^i$) and iii) convection of heat by gas diffusion ($\mathbf{j}_k^g$).

$$\mathbf{q}_h = \mathbf{q}^T + \rho^i \omega_k^i E_{Tk}^i \mathbf{q}^i + E_{Tk}^i \mathbf{j}_k^g \tag{10}$$

where $\mathbf{q}^T$ is conductive heat flow expressed by Fourier Law eq.(11)

$$\mathbf{q}^T = -\lambda_T \nabla T \tag{11}$$

where the thermal conductivity λ_T is a function of the degree of saturation.

2.1.3. Mechanical balance equation

The mechanical force balance equation is given as:

$$div(\boldsymbol{\sigma}^{\mathbf{tot}}) + \mathbf{b} = 0 \tag{12}$$

where $\boldsymbol{\sigma}^{\mathbf{tot}}$ is the total stresses and $\boldsymbol{b}$ denotes the body forces which typically is the self-weight of the material that relates to its bulk density (ρ^b). For evaluating soil stresses due to thermo-hydro-mechanical loading, an extended version of BBM soil model is used which is further described below in section 2.2.1.

2.2. Influence of temperature change

This section lists and overviews the constitutive relationships that enable thermal coupling on mechanical (section 2.2.1) and hydraulic (section 2.2.2) processes that are under consideration. Since the idea is to study the less explored thermal processes, the study does not investigate some of the thermal relations as those we believe to be fundamental in a THM model and well understood (for example, thermal conductivity factor, latent heat of vaporization or specific heat capacity). Further, the test simulations assume zero gas pressure head (h_g), thereby neglecting the contribution of dissolved air and limiting the scope in the gas phase. However, the study accounts for vapour production and movements enabled by liquid mass conservation (eq. 3), diffusion law (eq. 5) and heat conservation law (eq. 7).

2.2.1. Influence of temperature change on the mechanical behaviour of bentonite

To evaluate stresses and deformation in unsaturated materials, Thebes incorporates a modified version of BBM model that accounts for thermal effects. In the model the total elastic strain rate ($\dot{\boldsymbol{\varepsilon}}_{\mathbf{e}}$) is expressed as follows:

$$\dot{\boldsymbol{\varepsilon}}_{\mathbf{e}} = \dot{\boldsymbol{\varepsilon}}_{\mathbf{e}}^{\boldsymbol{\sigma}} + \mathbf{m}^T \dot{\varepsilon}_e^s + \mathbf{m}^T \dot{\varepsilon}_e^T \tag{13}$$

where, $\dot{\boldsymbol{\varepsilon}}_{\mathbf{e}}^{\boldsymbol{\sigma}}, \dot{\varepsilon}_e^s, \dot{\varepsilon}_e^T$ are elastic strains rates due to net stresses, suction and temperature, respectively, while $\boldsymbol{m}$ is a vector {1, 1, 1, 0, 0, 0}. Note, the model assumes that suction and temperature contribute to volumetric strains only. The net stress rate ($\dot{\boldsymbol{\sigma}}$) is represented as:

$$\dot{\boldsymbol{\sigma}} = \mathbf{D}^{\mathbf{e}} \dot{\boldsymbol{\varepsilon}}_{\mathbf{e}}^{\boldsymbol{\sigma}} = \mathbf{D}^{\mathbf{e}} \left(\dot{\boldsymbol{\varepsilon}}_{\mathbf{e}} - \mathbf{m}^T \dot{\varepsilon}_e^s - \mathbf{m}^T \dot{\varepsilon}_e^T \right) \tag{14}$$

where $\mathbf{D}^{\mathbf{e}}$ is the elastic stiffness matrix.

To better replicate the material behaviour, the elastic parameters vary with suction and pressure (Hoffmann et al., 2007) as shown in eq. (15) and (16):

$$\kappa = \kappa_o (1 + \alpha_\kappa s) \tag{15}$$

where κ is the swelling index with respect to net stress and κ_o is its

reference value. α_κ is a material constant that relates κ to matric suction (s). A minimum value $\kappa = 0.001\kappa_o$ applies to the above in case of large suctions leading to unrealistic negative κ values.

$$\kappa_s = \kappa_{so} \left[1 + \alpha_{\kappa s1} ln \left(\frac{p}{p_{ref}^c} \right) \right] e^{\alpha_{\kappa s2} s} \tag{16}$$

where κ_s, κ_{so} is the swelling index with respect to suction and its reference value, respectively, while $\alpha_{\kappa s1}, \alpha_{\kappa s2}, p_{ref}^c$ are material constants and p is the mean net stress.

The modified BBM model used here incorporates temperature dependency. This study examines the influence of thermal-mechanical couplings (i – iii):

i. The coupling between temperature (T) and (volumetric) elastic strain rate ($\dot{\varepsilon}_e^T$) is assumed as (Gens, 1995; Sánchez et al., 2012):

$$\dot{\varepsilon}_e^T = \frac{(\alpha_0 + \alpha_2(T - T_0))\dot{T}}{3} \tag{17}$$

where α_0, α_2 are material constants and T_0 is a reference temperature. As the simulations in the study (section 3) do not account for thermal strain variations due to the difference between actual and reference temperature ($T - T_0 = 0$), hence only α_0 is switched off (set to zero value) for the analysis.

ii. The coupling between the temperature and the size of the yield surface (Fig. 2). The yield criterion is:

$$F = q^2 - M^2(p + p_s)(p_0 - p) = 0 \tag{18}$$

where q and p are deviatoric and mean net stress, respectively and M is the slope of the critical state line. At a matric suction ($s = \rho_w^l g\psi$), p_0 is the pre-consolidation stress and p_s is a term that relates to suction induced increase in strength. In the considered modified version of BBM, p_0 and p_s are temperature dependent as shown in eq. (19) and (20).

The suction induced increase in strength p_s varies with temperature (Gens, 1995):

$$p_s = kse^{-\rho^T \Delta T} \tag{19}$$

where k and ρ^T are material constants. Based on the above equation and yield surface in Fig. 2, ρ^T governs the amount of change in the yield curve. Therefore, to examine the coupling it is
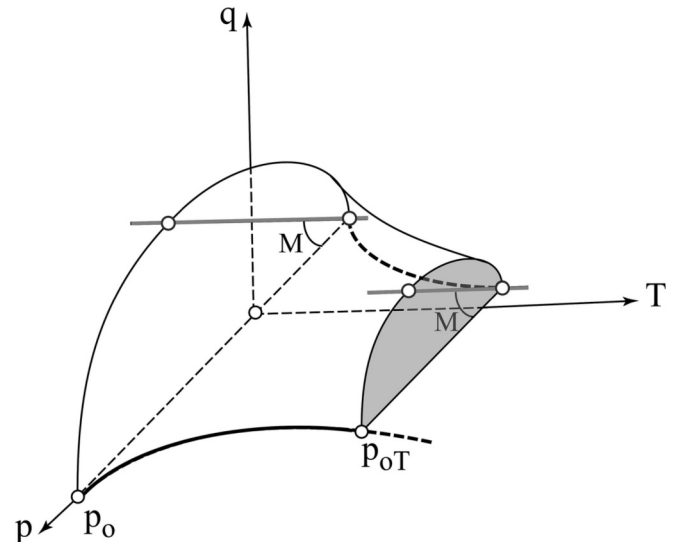
Fig. 2. Yield surface in (p, q, T) space (Abed and Sołowski, 2017).

set to zero.

iii. The temperature also influences the saturated pre-consolidation pressure (Laloui and Cekerevac, 2003):

$$p_{0T}^* = p_0^* \left[1 - \gamma_T log\left(\frac{T - T_{ref}}{T_0 - T_{ref}} \right) \right] \quad (20)$$

where p_0^* is the pre-consolidation pressure at suction $(s) = 0$. T_0, T_{ref} is the initial and the reference temperature, respectively. γ_T is a thermal coupling material constant that influences the change in the yield curve (Fig. 2) and thus is analysed by setting it to zero.

2.2.2. Hydraulic behaviour related thermal couplings

With the bases of the mass balance equation for the water component, the paper examines the following thermo-hydraulic coupling relations:

i. The van Genuchten water retention curve expression (eq. 6) is affected by temperature through parameters (g_a, g_n and g_m), see Jacinto et al. (2009):

$$g_a = (\sigma_0^t/\sigma^t)g_{ao}; \ g_n = \frac{g_{n0}}{1 - \xi_n^T g_{n0}(T - T_0)}; \ g_m = \frac{1}{g_n} - 1 \quad (21)$$

where g_{ao}, g_{n0} are the respective reference values. σ_0^t, σ^t are the surface tensions at reference temperature (T_0) and absolute temperature T, respectively. ξ_n^T is a material constant. Additionally, the degree of saturation at zero suction (S_{s0}^l) depends on temperature as follows (Jacinto et al., 2009):

$$S_{s0}^l = S_{sat}^l + \xi_w^T(T - T_0) \quad (22)$$

where ξ_w^T is another material constant.

To remove temperature dependency of the water retention curve, the analysis sets the expressions g_a and g_n (eq. 21) constant to their reference values and ξ_w^T equal to zero (eq. 22). Reviewing eq. (3), it influences the following terms: $\left[n\rho_w^l \frac{\partial S^l}{\partial T} \frac{\partial T}{\partial t} \right]$ and $\left[-n\rho_w^g \frac{\partial S^l}{\partial T} \frac{\partial T}{\partial t} \right]$.

As shown in Fig. 3, with the increase in temperature, these terms represent a loss in liquid water mass and the subsequent vapour mass gain, respectively. Conversely, as temperature decreases, the terms will represent condensation and a water mass gain. It is to be noted that since $S^g = 1 - S^l$, the part $-n\partial S^l/\partial T$ represents the equal and opposite change in volume of the gas phase. Hence, removing the temperature effect on the water retention curve affects the condensation and evaporation of water in the solution.

ii. The variation in liquid water mass due to the water density change, expressed in eq. (3) with the term: $\left[-nS^l\beta_{wT}\rho_w^l \frac{\partial T}{\partial t} \right]$. Physically, for a constant volume of soil, it represents the outflow of the water from the soil matrix. The expression is dependent on the coefficient of thermal expansion of water (β_{wT}), which is set to zero to remove the coupling.
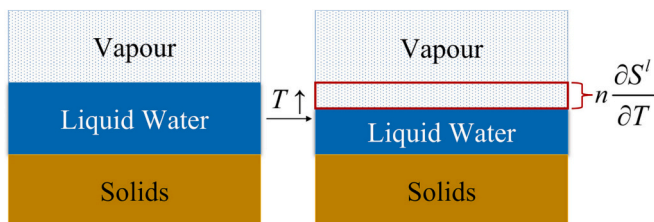

Fig. 3. Change in water and vapour masses due to coupling between the degree of saturation and temperature.
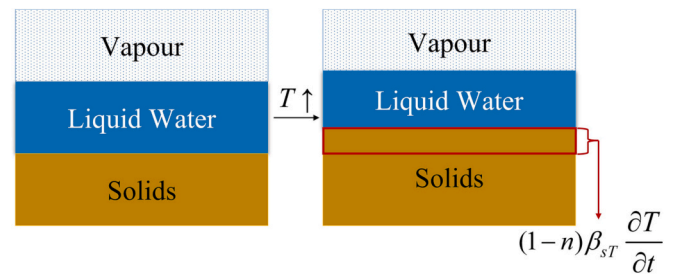

Fig. 4. Change in water and vapour masses due to change in solids via its thermal expansion.

iii. Thermal expansion of solids due to temperature, approximated as: $\left[-(1-n)(S^l\rho_w^l + S^g\rho_w^g)\beta_{sT}\frac{\partial T}{\partial t} \right]$, with β_{sT} being the governing constant. Setting it to zero removes the coupling. As shown in Fig. 4, the above term represents the change in fluid mass due to the volumetric expansion of solids. The expression represents an outflow of both water and vapour masses in a unit element.

iv. The effect of temperature on relative humidity and suction equilibrium condition. Relative humidity (RH) is the ratio between the actual vapour density (ρ_w^g) in the air by the maximum saturated vapour density (ρ_{w0}^g). In unsaturated porous medium, through Kelvin's law, relative humidity is also in thermal equilibrium with suction, the function is expressed as (Rutqvist et al., 2001):

$$RH = \rho_w^g / \rho_{w0}^g, RH = e^{\frac{-gM_w\psi}{RT}} \quad (23)$$

where ψ is a suction head and T is for temperature. Making relative humidity and suction equilibrium condition constant with temperature ($T = T_0$, using initial simulation temperature in eq. 23), affects the vapour density differential eq. (24) and vapour diffusion coefficient eq. (25) and (26). In this case terms: $\left[\frac{gM_w}{R} \rightarrow 0 \right]$, $\left[\frac{gM_w}{RT}, \text{where } (T = T_0) \right]$ are affected in eq. (3).

$$\frac{\partial \rho_w^g}{\partial t} = \frac{\partial \rho_w^g}{\partial T}\frac{\partial T}{\partial t} + \frac{\partial \rho_w^g}{\partial \psi}\frac{\partial \psi^l}{\partial h_g}\frac{\partial h_g}{\partial t} + \frac{\partial \rho_w^g}{\partial \psi}\frac{\partial \psi^l}{\partial h_w}\frac{\partial h_w}{\partial t}$$
$$= \frac{\rho_w^g}{T^2}\left(4974.0 + \frac{gM_w\psi}{R} \right)\frac{\partial T}{\partial t} + \frac{\rho_w^g gM_w}{RT}\left(\frac{\partial h_w}{\partial t} - \frac{\partial h_g}{\partial t} \right) \quad (24)$$

$$D_{vw} = D_{atm}v_v\tau\phi^g\rho_w^g\frac{gM_w\psi}{RT} \quad (25)$$

$$D_{vT} = f_{Tv}D_{atm}v_v\phi^g\tau\rho_w^g\left[\frac{4974}{T^2} + \frac{gM_w\psi}{RT^2} \right] \quad (26)$$

where f_{Tv} is the thermal enhancement factor, D_{atm} is a molecular diffusivity of vapour, v_v is a mass flow factor and τ is the tortuosity. The numeric value (4974) in eq. (24, and 26) is the result of partial differential of empirical relation of saturated vapour density with respect to temperature eq. (27).

v. The effect of temperature on the saturated water vapour density. In eq. (23) the relative humidity (RH) is further dependent on reference saturated density (ρ_{w0}^g), which is expressed as (Wang et al., 2009):

$$\rho_{w0}^g = 10^{-3}e^{19.891 - \frac{4974.0}{T}} \quad (27)$$

To remove the coupling, a constant initial simulation temperature ($T = T_0$) is used in the above equation. In the Thebes framework the coupling affects terms: $[4974.0 \rightarrow 0]$, $\left[\frac{4974}{T^2} \rightarrow 0 \right]$ in eq. (6), (24) and (26).

Table 1

Test configuration.

Test	Thermal couplings	Remarks
Baseline model	–	All thermal couplings are active
T1	α_0	BBM parameter enabling temperature related elastic strain (eq. 17) is set to zero (see, section 2.2.1- i).
T2	ρ^T	BBM parameter enabling thermal induced yielding (eq. 19) is set to zero (see, section 2.2.1- ii).
T3	γ_T	Parameter controlling yield curve (eq. 18) is set to zero (see, section 2.2.1- iii).
T4	Van G.(T)	van Genuchten water retention curve expression (eq. 6) is turned isothermal by making expressions g_α and g_n (eq. 21) constant to their reference values and setting ξ_w^T (eq. 20) to zero (see, section 2.2.2 - i).
T5	β_{wT}	Parameter enabling thermal expansion of water is set to zero (see, section 2.2.2 - ii).
T6	β_{sT}	Parameter enabling thermal expansion of soil solids is set to zero (see, section 2.2.2 - iii).
T7	$\rho_w^g(\text{RH}\_\psi, \text{T})$	Vapour density as a function of relative humidity and suction thermal equilibrium condition (eq. 23) is made isothermal, by making relative humidity constant to the initial simulation temperature (T_o). See, section 2.2.2 - iv.
T8	$\rho_w^g(\rho_{w0}^g, \text{T})$	Vapour density as a function of saturated vapour density and temperature (eq. 27) is made isothermal, by making the expression constant to the initial simulation temperature (T_o). See, section 2.2.2 - iv.
T9	$D_{atm}(T)$	Molecular vapour diffusive coefficient is made isothermal by making the expression (eq. 28) constant with initial simulation temperature (T_o). See, section 2.2.2 - v.
T10	$\mu_l(T)$	Viscosity expression (eq. 29) is made isothermal by making it constant with initial simulation temperature (T_o). See, section 2.2.2 - vii.

vi. Effects of temperature on molecular diffusivity. The framework employs De Vries (1987) expression for molecular diffusivity:

$$D_{atm} = 2.16 \times 10^{-5} \left(\frac{T}{T_{ref}} \right)^{1.8} \tag{28}$$

where T_{ref} is a reference temperature (273.16 K). A constant molecular diffusivity ($T = T_0$, in eq. 28) can reduce the vapour flux ($\mathbf{j}_w^g$) at high temperatures. Thus, this paper examines the influence of the temperature by keeping D_{atm} constant, with the value computed for the temperature T set to the initial simulation temperature (T_o).

vii. The liquid viscosity (μ_l) is affected by temperature (van Esch, 2010):

$$\mu_l = \left(243.18 \times 10^{-7} \right) 10^{\frac{247.8}{T-140}} \tag{29}$$

Lack of temperature dependency should reduce the liquid flux at higher temperatures. This is evaluated in the current study by making viscosity constant to the initial simulation temperature (T_o).

2.3. Test configuration

Table 1 shows the list of ten simulation setups (T1-T10), each with one thermal coupling inactive. The setups are used to simulate again 2 experiments, the non-isothermal infiltration test and the CIEMAT mock-up test. In each of those cases, the differences between the results of simulations with inactivated thermal coupling and the baseline model simulation allow for assessing how important the coupling (T1-T10) is in the experiment.

3. Analysis of the influence of thermal coupling components on the simulation outcome

The following section presents results and a thorough discussion of the infiltration and mock-up test simulations. For each test scenario, we discuss baseline simulations in Thebes first (section 3.1.1 and 3.2.1), followed by respective thermal coupling analysis (section 3.1.2 and 3.2.1). To increase clarity and readability, we present the results using the sign conventions adopted in soil and rock mechanics, i.e., utilizing positive signs for compressive stress and strain.

3.1. Non-isothermal infiltration test

The study bases on Abed and Sołowski (2017) FEM simulation of a non-isothermal hydration experiment on bentonite (Villar and Gomez-Espina, 2009). In the experiment, Febex bentonite (dry density of 1.65 g/cm^3) was set up in a cylindrical cell measuring 40 cm in length and 7 cm in diameter (see, Fig. 5). To replicate nuclear repositories THM conditions, the cell has simultaneous heating at the bottom and a water inlet at the top.

Thebes FE simulation uses an axisymmetric model with 0.4 m length and 0.035 m width. The model is meshed with 250 quadrilateral 4 noded elements (4 - gauss integration points), as shown in Fig. 6 c.

To replicate the experiment more accurately, the simulation takes into account the layers that bound bentonite: thin layer of Teflon, triaxial cell steel and foam. These materials are modelled as a non-
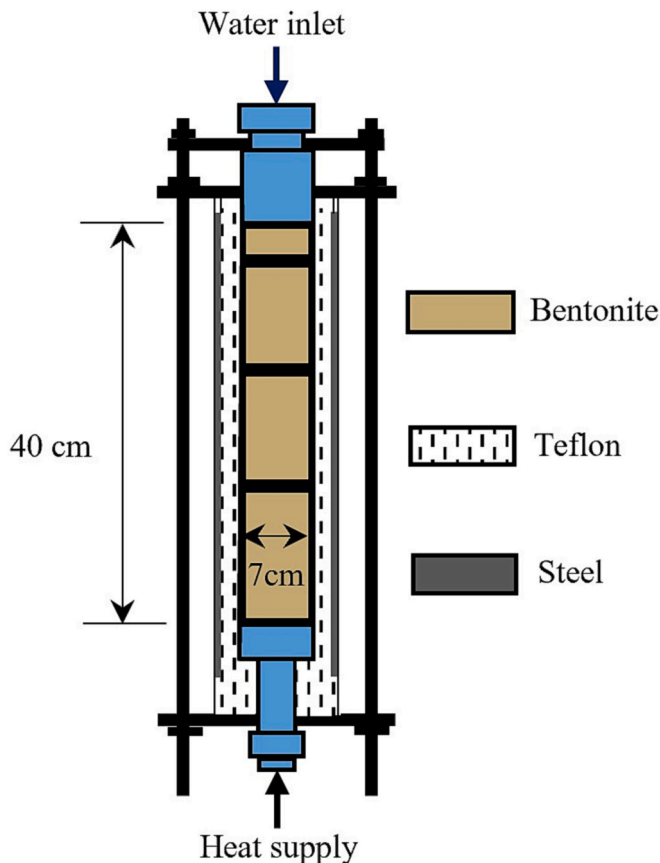

Fig. 5. Experimental setup of infiltration test (modified from Villar and Gomez-Espina, 2009).
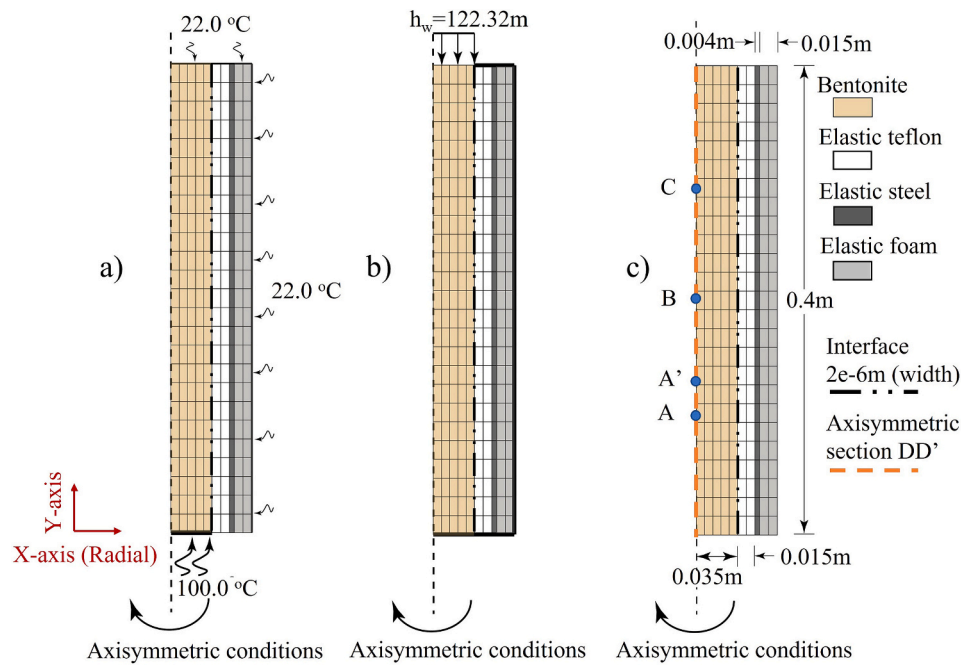
Fig. 6. Finite element model for non-isothermal infiltration test: a) Thermal boundary conditions, b) Hydraulic boundary conditions, c) Dimension of the geometry, controlled points and section. (modified from Abed and Sołowski, 2017).

Table 2
Material properties (Abed and Sołowski, 2017).

Material	Young's modulus (E) [kPa]	Poisson ration (υ)	Thermal Conductivity (λ_T) [W/m.K]
Teflon	5.0e+5	0.46	0.25
Steel	2.0e+8	0.3	12
Foam	1.0e+4	0.3	0.17
Interface	100	0.499	200

Table 4
Hydraulic properties of soil, infiltration test.

g_{a0} [1/m]	g_{n0}	S_{res}^l	S_{sat}^l	ξ_n^T [1/K]	ξ_w^T [1/K]	K_{sat}^l [m/s]
12.0e-4	1.22	0.01	1.0	−1e-4	-1.5e−3	1.9e−14

K_{sat}^l is hydraulic conductivity at full saturation.

Table 5
Thermal properties of soil, infiltration test.

λ_{sat} [W/m.K]	λ_{dry} [W/m.K]	τ	f_{Tv}	c_s [J/kg.K]	c_w^l [J/kg.K]	c_w^g [J/kg.K]
1.15	0.47	0.8	1.0	1000.0	4180	1900

λ_{sat}, λ_{dry} are thermal conductivity at the fully saturated and dry state, respectively. c_s, c_w^l and c_w^g are specific heat of soil, water, and vapour, respectively.

Table 6
Phase properties, infiltration test.

ρ_{wo}^l [kg/m³]	β_{wp} [1/pa]	ρ^{so} [kg/m³]	β_{sT} [1/K]	β_{wT} [1/K]
998.2	4.58e-10	2700.0	7.80E-6	2.10E-4

ρ^{so} is a reference solid particle density.

porous linear elastic, with Table 2 listing the mechanical and thermal properties of external layers.

The simulation modifies the model by Abed and Sołowski (2017) with an inclusion of an interface layer (2e-6 m thick) to better account for the low friction between the bentonite and Teflon layers, see Fig. 6. The layer is assumed to be a non-porous linear elastic material with high thermal conductivity, refer to Table 2, for properties. The interface layer is thin enough that it has a negligible effect on radial deformability or stresses. For example, we estimate that the maximum error is around 0.006% in radial compressive strain.

The simulation replicates the initial temperature in the experiment (22 °C). The bentonite initial mean net stress is 1.0 kPa and suction is 120 MPa. Other boundary conditions in the simulation are set as shown in Fig. 6.a and b. The top and side of the sample temperatures are set to 22 °C, whereas the bottom has its temperature set to 100 °C. The flow boundaries are closed. However, after 66 h of simulation, the top boundary condition changes with a constant pressure head of 122.32 m

Table 3
Mechanical properties of soil, infiltration test.

ν	κ_o	κ_{so}	n	α_0 [1/K]	α_2	α_k	α_{ks1}	α_{ks2}	M	k
0.4	0.05	0.3	0.4	1.5e-4	0.0	-3.0e-6	−0.147	0.0	1.5	0.1
p_{ref}^c [kPa]	λ	β [1/kPa]	r	γ^T	ρ^T	p_o^* [kPa]				
13.0	0.15	5.0E-5	0.75	0.25	0.2	1.4e+4				

ν is the Poisson's ratio, M is the slope of the critical state line. λ, β, and r, are BBM parameters.
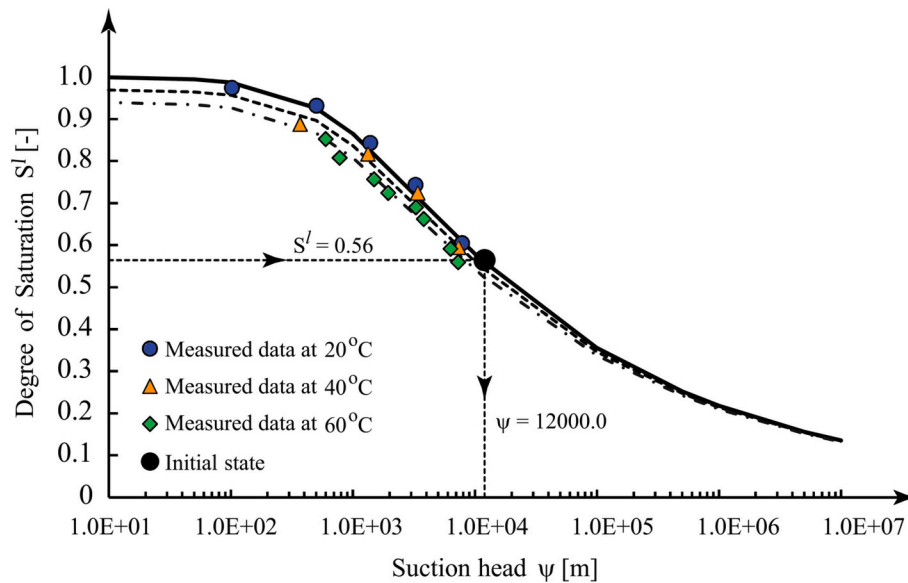
Fig. 7. Retention curve at different temperatures fitted in Thebes for the simulation (modified from Abed and Sołowski, 2017).

prescribed. The simulation assumes zero gas pressure during the whole simulation and vapour flow is taken as diffusive only, the test does not require the specification of gas boundary conditions.

Simulation constrains radial direction movements on the right side of the interface (next to Teflon) as well as any boundary movements on top and bottom. There are three data collecting points along the axisymmetry line DD' at heights Y = 0.3 m (A), 0.2 m (B) and 0.1 m (C), see Fig. 6 c.

The soil properties shown in Table 3-6 are taken from Abed and Sołowski (2017). These are calibrated based on studies by Villar et al., 2008 and Sánchez et al., 2012. Further, the van Genuchten parameters are fitted as per the retention curve data shown in Fig. 7.

3.1.1. Infiltration test: Baseline model case analysis

To facilitate the comparisons between the thermal coupling and baseline model along the axisymmetric line DD', the section provides a critical analysis of the results under a fully active formulation. It is worth mentioning, reader may refer to Abed and Sołowski (2017) for the validation study of Thebes's baseline model against the infiltration
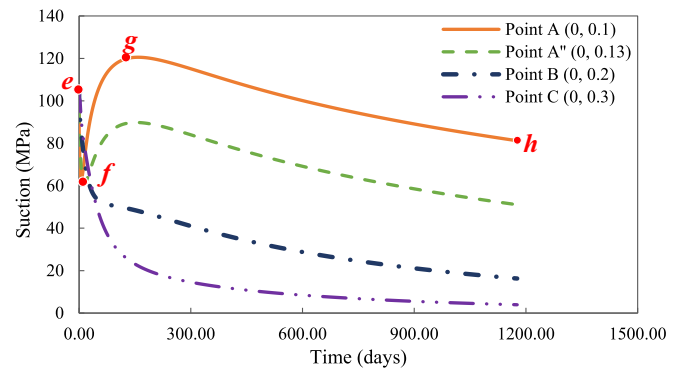
Fig. 9. Suction evolution during the infiltration test.
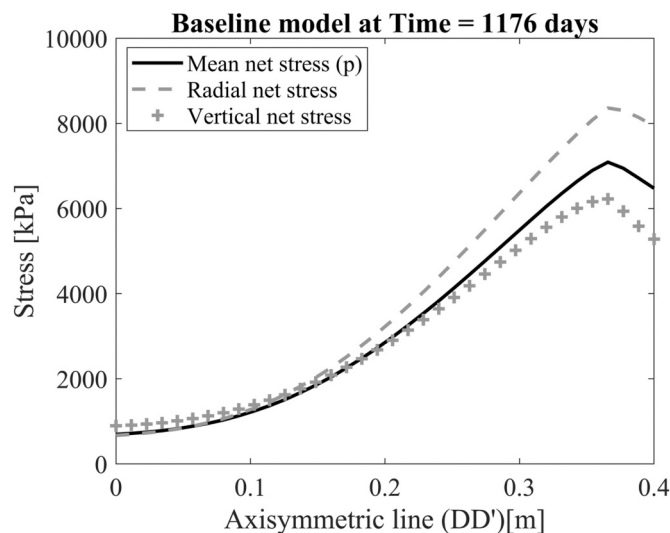
experiment. Fig. 8, shows the mean net stress p profile along the axisymmetric line (DD') at the end of the simulation ($t = 1176$ days). Examining the figure reveals that swelling pressure in bentonite develops due to the hydration and related reduction in suction (see, Fig. 9), as the sample is constrained at constant volume.

Closer to the hydrating boundary side the swelling pressure builds up to approximately 7.7 MPa (mean net stress value), whereas at the dry side mean net stress increases up to 1 MPa. The noticeable post-peak reduction of stresses at the wetting boundary is due to the positive sign of the pore water pressures as that part of bentonite reaches its full saturation state (see, supplementary data Fig. S1) and net stress becomes the classical Terzaghi's effective stress in this region.

The analysis of the vertical (σ_y) and radial (σ_r) (see, Fig. 8) stress components along the axisymmetry line shows that they contribute towards the mean stress almost equally, with the radial net stress being slightly higher near the wetting side perhaps due to the differences in the boundary proximity along the radial and vertical directions. Additionally, along any radial line (see, supplementary data Fig. S2), the value of radial stresses remains. In other words, during the simulation, the variation in radial stress occurs along the y-axis in response to the thermal and hydraulic boundaries but remains quite uniform along any radial cross-section.

Apart from stress states at the end of the simulation, the suction profiles shown in Fig. 9 highlight the time-dependent response of bentonite at points A, B and C. Besides shown data points in Fig. 6, an

Fig. 8. Infiltration test stresses: isotropic net stress (p) (swelling pressure), vertical net stress (σ_y), radial net stress (σ_r).

additional point A" (0, 0.13) is observed to further investigate and classify bentonite behaviour based on the upper, middle and lower regions of the column. There is a gradual decrease in suction values near the wetting boundary (Point C) and around the mid-section regions (Point B) throughout the time, thus indicating a continuous hydration process. However, in contrast to the former locations, near the heating side at points A and A" the suction evolution is more complex. Suction at points A and A" at the *Initial stage* reduces (Fig. 9, e-f), then increases in the *Transition stage* (Fig. 9, f-g) and finally gradually decreases in the *Post-transition stage* (Fig. 9, g-h).
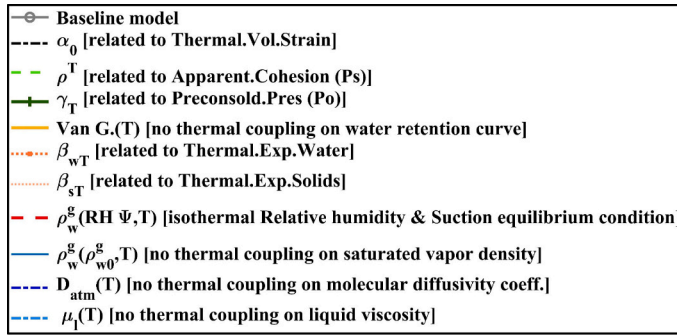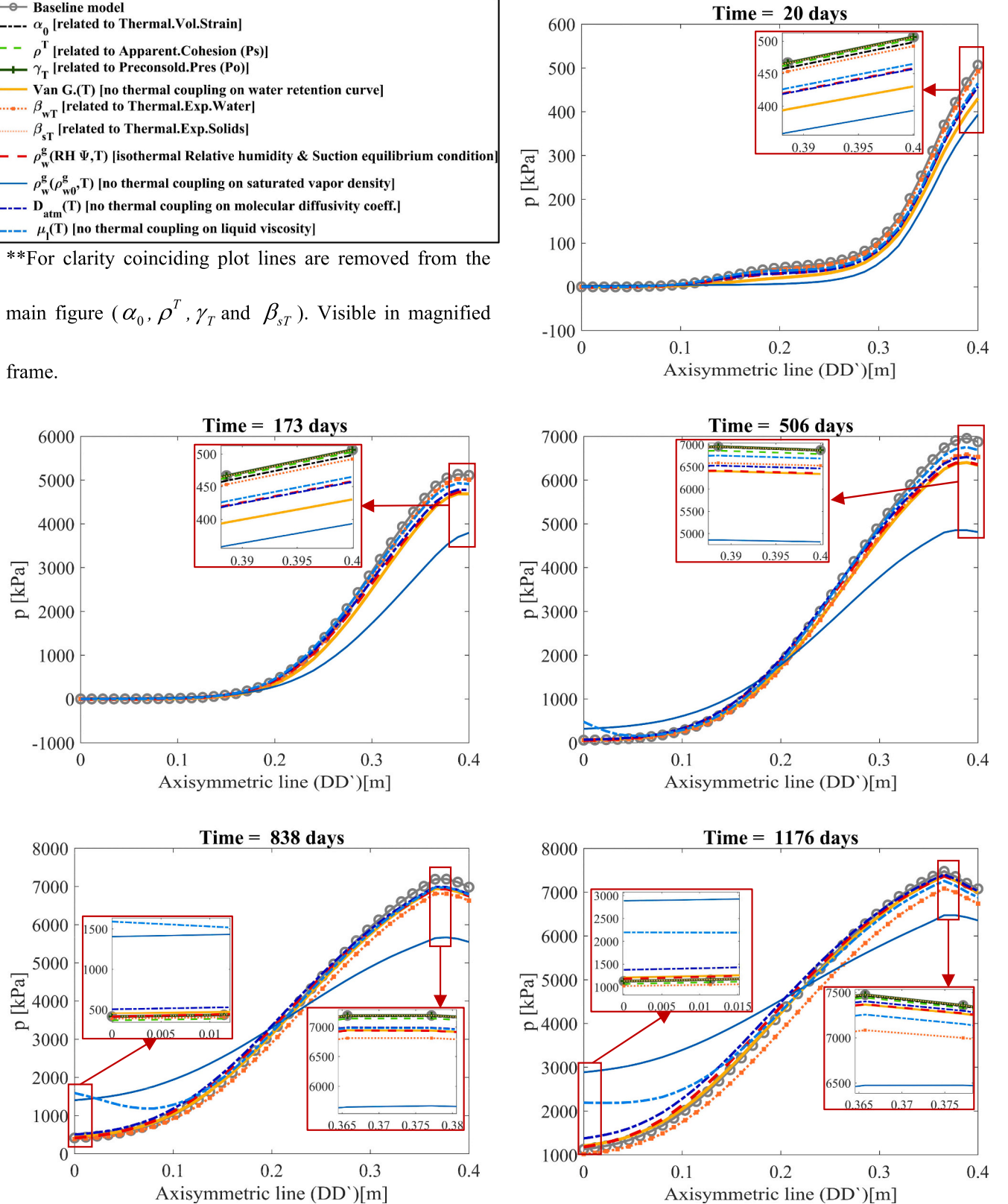
Fig. 10. Mean net stress (swelling pressure) *p* in Infiltration test at different times, along axisymmetric line (section DD').

In the *Initial stage* suction near the heated boundary reduces during the first 5 days (section e-f in Fig. 9). During that time the wetting boundary is initially inactive (first 2.7 days). The drop in suction values during this stage throughout the bentonite is predominantly governed by vapour movement from the heating side and its subsequent condensation. As a result, suction at points A and A" show the steepest decline followed by mid-region (point B) and eventually point C. During the *Transition stage* suction rises around the heated boundary at points A and A", whereas elsewhere suction reduces (Fig. 9, f-g, days 5 to 160). In the *Transition stage* water (liquid) from the wet boundary still has not penetrated the lower regions of the bentonite domain. On the other hand, the temperature increase progresses from the heating side, leading to lower relative humidity, higher suction, as well as evaporation and vapour transport. Afterwards, during the *Post-transition stage* suction drops in all the locations (Fig. 9 g-h). At this time water (liquid) from the wetting side penetrates the lower drier regions of bentonite and hydrates them.

3.1.2. Infiltration test: Thermal coupling analyses

Figs. 12 - 16 show the results of the simulations with selected couplings disabled. We analyse the results below, starting with the thermal couplings most significantly affecting results. We removed the plot data lines of thermal couplings that almost coincided with the baseline model
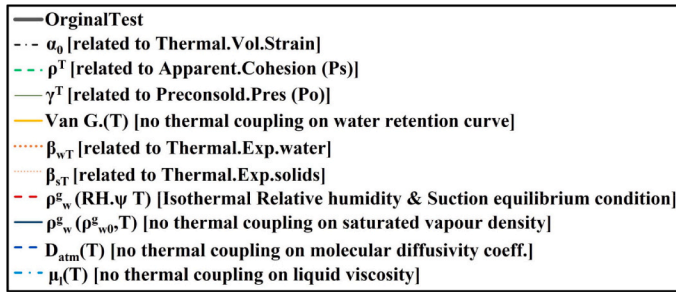
simulation from the main figure to maintain clarity and avoid clustering. However, they are kept in the magnified frames. For the complete set of net mean stress results versus time for all the thermal couplings, refer to the supplementary data (MeanStress_InfiltrationTest.avi).

a) *Vapour density thermal coupling concerning reference saturated density* $[T8 - \rho_w^g(\rho_{w0}^g, T)]$ –The absence of vapour density coupling significantly impacts bentonite swelling pressure, with the peak difference of about 155% (vs baseline model) at $t = 1176$ days (Fig. 10). It also leads to a lower suction value closer to the heating side indicating a higher degree of hydration at the lower parts of bentonite Fig. 11.a.

Reviewing the associated terms of the coupling in a numerical framework provides insights into the physical mechanisms leading to such a significant effect. Eq. (27) describes how the saturated vapour density (ρ_{w0}^g) increases with the temperature rise. Consequently, that affects the evaporation process through eq. (24) and eq. (26), which implies an increase in vapour mass and an increase in the rate of vapour diffusivity, respectively.
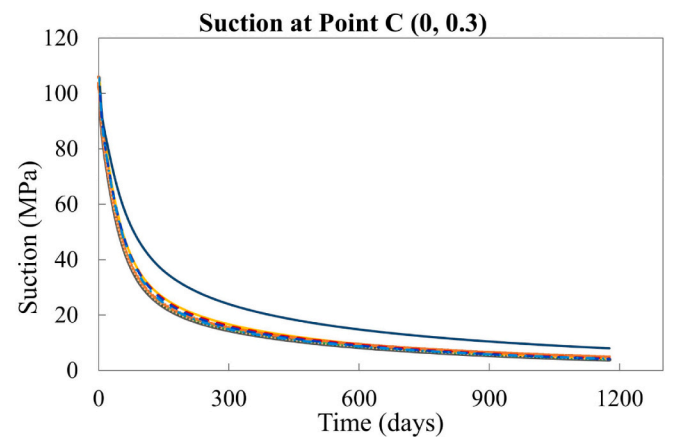
Conversely, the absence of thermal coupling in reference saturated density results in a lower evaporation rate, which leads to a greater extent of hydration (see near heating side Fig. 10). However, reduced evaporation also suggests a lower contribution of condensation on bentonite hydration. The effect is most notable in the upper regions
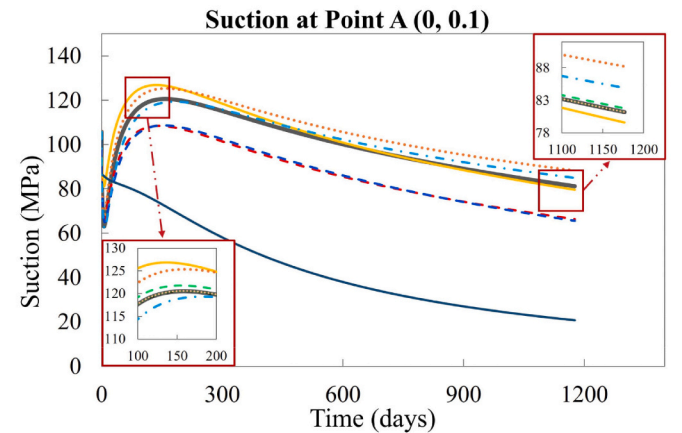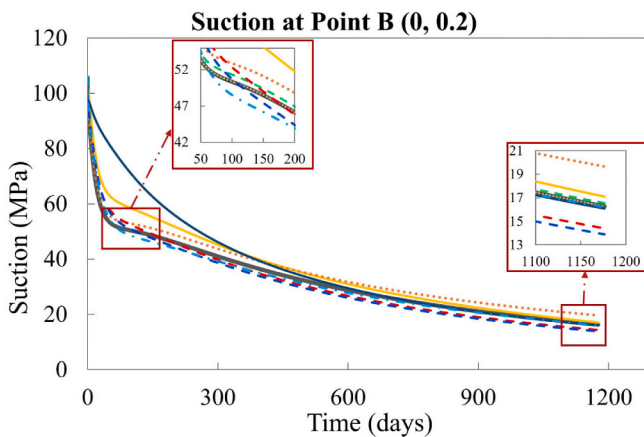
Fig. 11. Suction vs time in the infiltration test, at selected points: a) at Point A, b) at Point B, and c) at Point C.
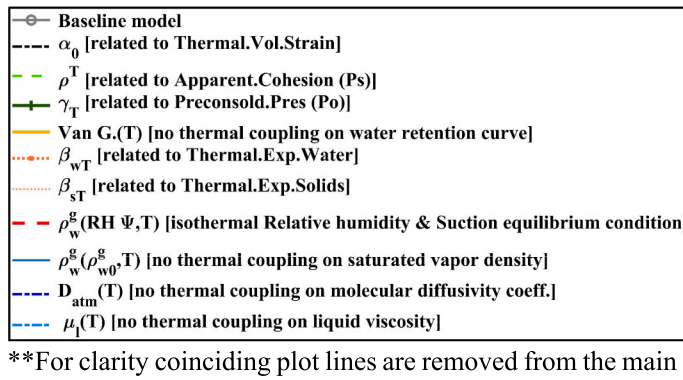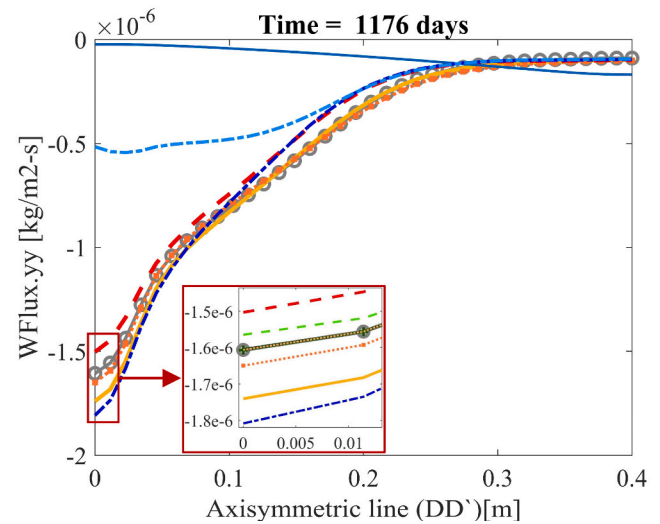
12

Fig. 12. Water mass flux in y-direction in the infiltration test (negative sign represent a downward flow)

of bentonite, as evident from the lower rates of suction drop shown in Fig. 11.b and c. Hence, the difference in hydration behaviour in the bentonite column leads to a mean stress pattern of relatively higher values at the bottom regions and lower values at the upper parts (see, Fig. 10). Since the above results highlight the importance of vapour in the model, it led us to examine the full extent of the vapour effect on the simulation. It is done by performing an additional case of an uncoupled vapour flow model and comparing it with the baseline model. Refer to supplementary data (section S.3) for the results and discussion of the case.

b) *Liquid viscosity thermal coupling [T10 - $\mu_l(T)$]* – As discussed in section 2.2.2 (vii), the absence of the viscosity coupling primarily impacts liquid mass flux in the water mass balance eq. (3). Similarly as observed by Schäfers et al. (2020), Fig. 12 shows that taking the viscosity of liquid as constant leads to a much slower water mass flux than in the baseline case, where the viscosity of water decreases with the temperature rise. This is expected, as the temperature in the analysed case increases in the domain, hence the viscosity reduction is equivalent to an increase in the permeability of bentonite. Even though the suction is not affected very much in % terms, see Fig. 11.
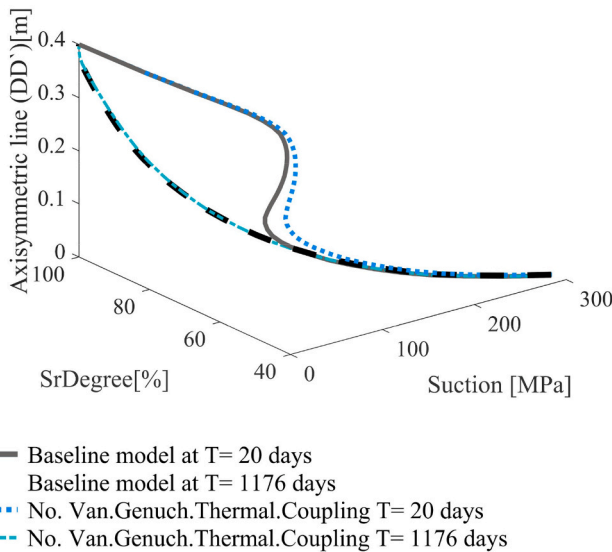
Fig. 13. Retention curve along the axisymmetric line for infiltration test: baseline model vs isothermal van Genuchten test case.

a, the constant viscosity of liquid and associated smaller flows of liquid water through bentonite leads to a higher mean stress in the dry region of a soil column. Figure Fig. 10 shows a peak difference of about 1000 kPa at $t = 838$ days (vs baseline model). This anomaly might suggest influences of other physical processes and couplings (2nd order effects), which requires further assessment in future.

c) *van Genuchten Temperature coupling [T4 - Van G.(T)]* – In the case of the isothermal van Genuchten water retention curve, the mean stress result deviates more from the baseline model closer to the beginning of the experiment, with a peak difference of approximately 15% at day 20 (see, Fig. 10). The difference reduces to about 8% at mid-stages (t = 838 days) and later to <2% at the end of the simulation. The behaviour is strongly dependent on the water retention curve, as can be observed in Fig. 13. The figure shows a higher difference in retention curves between the trial case and the baseline simulation at the 20-day mark, which eventually diminishes at the end of the simulation.

d) *Thermal coupling due to molecular diffusivity factor [T9 - $D_{atm}(T)$]* – As temperature rises in the simulation, keeping the molecular diffusivity constant leads to changes in vapour flux patterns in the soil column. Fig. 14 indicates lower vapour flux in the upper and mid part of the soil column and higher at the bottom (near the heated side). The lower vapour flux is due to lower molecular diffusivity. However, the higher vapour flux at the bottom is due to the large suction gradient (higher vapour mass concentration gradient), resulting from the uncoupling. Upon examination of suction values at points A and B (Fig. 11.a and b), point A experiences 15.6 MPa lower suction than the baseline model case, whereas at point B, the difference is only 2.4 MPa. Hence, the phenomenon dominates around the drier part of the soil column, where suction is high.

The influence of vapour movement reflects in the mean net stress (see, Fig. 10), where the bottom region shows higher stress values peaking at t = 1176 days by 21%, and the upper soil region shows lower stress values peaking at $t = 20$ days by 9% (vs baseline model). The higher vapour flux movement at the bottom possibly leads to more hydration due to an increase in vapour condensation. Whereas, in the upper regions, the lower extent of vapour reach may result in less hydration. Later, the difference in the upper soil region reduces to <1% at the end of the simulation, as the contribution of vapour condensation decreases in time, with the increasing amount of water infiltration from the top.

e) *Thermal expansion of water [T5 -β_{wT}]* – Not considering the thermal expansion of water predominantly affects the simulation at later stages. Fig. 10 shows a peak difference of 6% at day 1176 (vs baseline
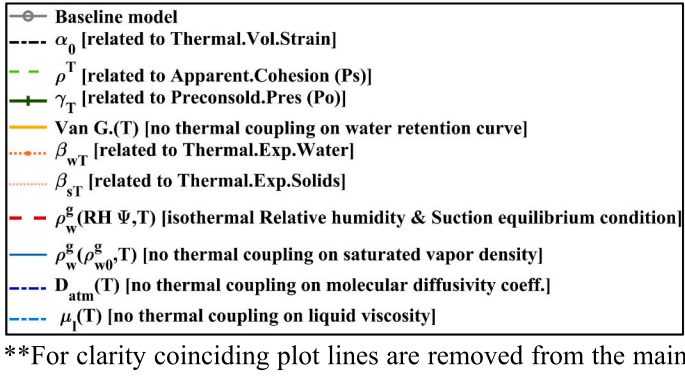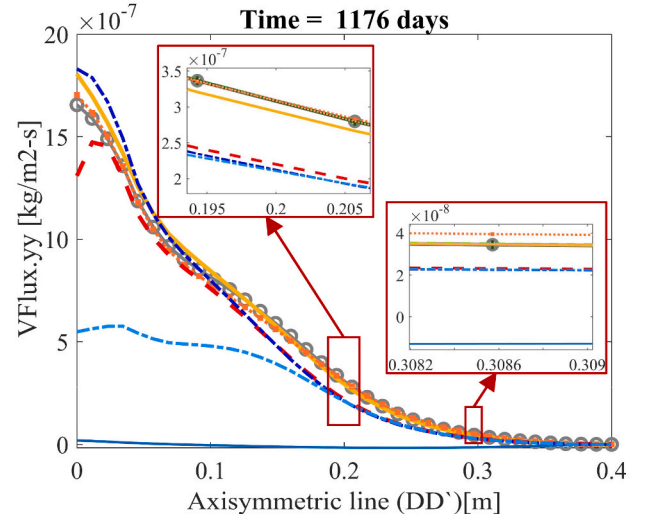
Fig. 14. Vapour mass flux during the infiltration test, in the y-direction along the axisymmetric line at t = 1176 days (positive sign represents an upward flow).

model) in mean stress. A likely explanation is that an increase in saturation over time will lead to more water getting affected by thermal expansion. Moreover, the results suggest that the absence of such coupling may influence other temperature dependent hydraulic processes, leading to higher suction in the soil column (Fig. 11) and higher flux movements (Fig. 12 and Fig. 14).

f) *Thermal coupling in relative humidity and suction equilibrium condition [T7 - $\rho_w^g(RH\_\psi, T)$]* – The uncoupling of temperature in relative humidity and suction equilibrium condition leads to lower vapour mass production and lower vapour movement (see, Fig. 14). It affects the hydration process in two ways:

1) Higher discrepancies at the upper regions of a soil column in mean effective stress results compared to the baseline model (Fig. 10). It may suggest lower hydration due to reduced vapour condensation at early stages. A peak difference of about 9.5% at t = 20 days is seen, which reduces to 1.5% at the end.

2) Relatively higher hydration at mid and bottom regions in later stages (vs baseline model), which may be due to lower resistance from the counter vapour mass production. Fig. 10 shows a peak difference of about 8% in mean effective stresses around lower-mid regions at the end of the simulation. Such discrepancies are also evident in suction in Fig. 11 that shows considerably lower values near the bottom (Fig. 11.a) and slightly lower values at the mid-point (Fig. 11.b), in later stages of the simulation.

g) α_0 *[T1], ρ^T [T2], γ_T [T3] and thermal expansions of solids [T6 - β_{sT}]* – Thermal uncoupling associated with these parameters shows <1% variation in mean effective stress (Fig. 10) and suction (Fig. 11), vs the baseline model. This is expected, as in the simulations no plasticity is observed. In elastoplastic simulations, the influence of γ_T cannot be completely ruled out.
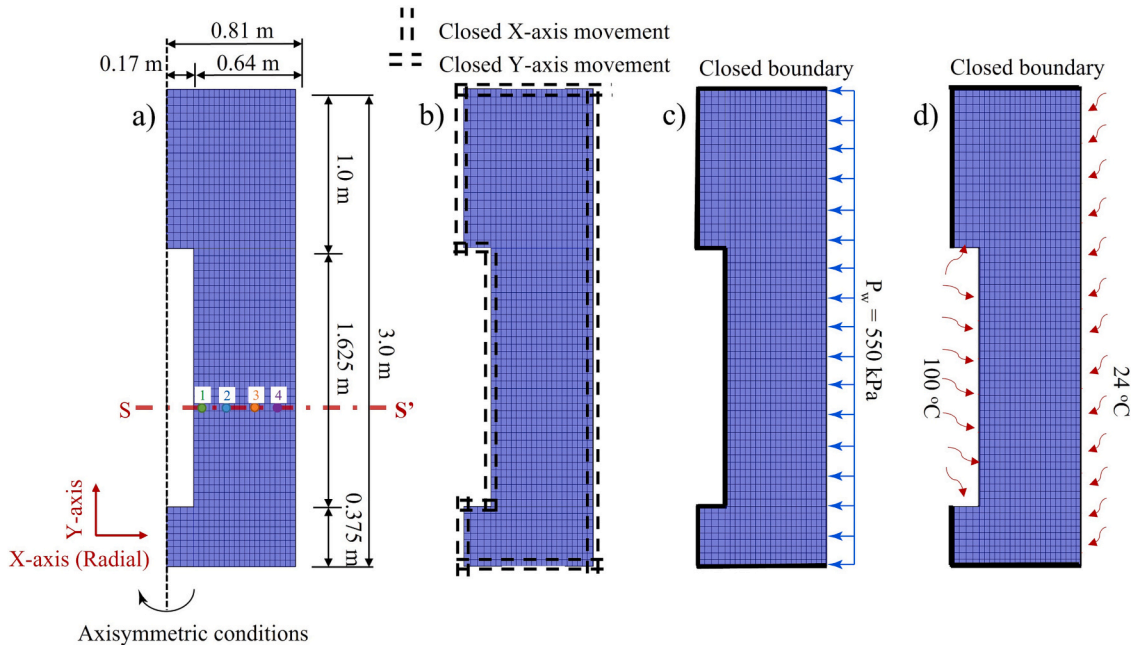

Fig. 15. Mock-up test FEM model; a) problem geometry, b) mechanical boundary conditions, c) hydraulic boundary conditions, d) thermal boundary conditions (modified from Abed and Sołowski, 2020).

3.2. Mock-up experimental test simulation

Under Febex and Febex II projects, CIEMAT (Madrid, Spain) set up a mock-up test (see, Fig. 15) on Febex bentonite with controlled boundaries, simulating deep geological nuclear repository test conditions (Martin et al., 2006). The test was designed to study the long-term behaviour of bentonite under the influence of thermal, hydraulic, and mechanical actions. The data acquired in this study is used as a reference to validate code Thebes (Abed and Sołowski, 2020).

Fig. 15.a shows the geometry and the finite element model. In total, 1396 four nodded quadrilateral elements with four integration points per element were used.

To ensure constant volume, the displacement boundaries were restrained from any movements in the normal directions (see, Fig. 15.b). To replicate experimental test conditions, a constant hydraulic pressure of 500 kPa is maintained on the wetting side of the test, keeping the other boundaries closed to water flow (Fig. 15.c). Additionally, similar to the infiltration test, the simulation does not require gas boundary constraint, as we assume zero gas pressure and diffusive vapour flow. Furthermore, a constant temperature of 100 °C is prescribed on the drying side and 24 °C on the wetting (Fig. 15.d). Replicating in the experiment, the heat in the drying boundary is increased gradually. The first 250 W of energy flux is maintained for initial 6 days, followed by 500 W up to 10 days thereby reaching 100 °C. Further, the simulation sets the bentonite initial temperature to 24 °C, its mean effective stress of 10 kPa (replicating the average self-weight of bentonite in the middle of the domain) and suction of 120 MPa. Fig. 15.a, shows four control points and a radial section line SS' where simulation data are read.

To simulate the Febex bentonite, soil properties shown in Table 7-10 are referred from Abed and Sołowski (2020). The hydraulic, mechanical and thermal properties are calibrated using data by Gens et al. (2009), Jacinto et al. (2009), Villar and Gomez-Espina (2009), and Sánchez (2014).

3.2.1. Mock-up Test: Baseline model case analysis

In this section, a comprehensive assessment of the baseline model case is presented solely for the purpose of comparing it with the deactivated thermal coupling scenarios discussed in the later section (section 3.2.2). However, to get insights on Thebes's baseline model performance against the Mock-up test experiment, readers are directed to Abed and Sołowski (2020).

Fig. 16 shows stress distributions along the radial section line SS' (Fig. 15) at the end of the simulation. Fig. 16.a, shows a peak mean effective stress of about 9.8 MPa. Moreover, from Fig. 16.b and c, it is observed that the variation of radial stress along the section line is relatively insignificant with the difference between maximum and minimum value being around 7%. It is the Y-axis stresses which cause the main difference in mean stresses along the section line. Similarly, as in the infiltration test, here as well the post-peak reduction in mean effective stress (swelling pressure) is due to the positive pore water pressures (see, supplementary data Fig. S3).

Fig. 17 shows the suction evolution at points 1–4 along radial section SS' throughout the simulation time. The test follows a similar pattern as the infiltration test. In the *Initial stage* suction falls suddenly closer to the heating side (section e-f, Fig. 17). At this phase, suction in the bottom regions falls more than in the upper region points thus indicating a predominant vapour condensation as a hydration mechanism. The stage ends after around 20 days, at which time the water from the wetting side

Table 8
Hydraulic properties of bentonite, Mock-up test.

g_{a0} [1/m]	g_{n0}	S_{res}^l	S_{sat}^l	ξ_n^T [1/K]	ξ_w^T [1/K]	K_{sat}^l [m/s]
3.5e-4	1.22	0.0	1.0	-1e-4	-1.5e-3	1.9e-14

Table 9
Thermal properties of bentonite, Mock-up test.

λ_{sat} [W/m. K]	λ_{dry} [W/m. K]	τ	f_{Tv}	c_s [J/kg. K]	c_w^l [J/kg. K]	c_w^g [J/kg. K]
1.15	0.47	0.87	1.0	920.0	4180	1900

Table 10
Phase properties, Mock-up test.

ρ_{wo}^l [kg/m³]	β_{wp} [1/pa]	ρ^{so} [kg/m³]	β_{sT} [1/K]	β_{wT} [1/K]
998.2	4.58e-10	2700.0	7.80e-6	3.40e-4

starts saturating the upper regions but has yet to reach near the heating side (*Transitional stage*). In this stage suction increases at points 1 and 2 and decreases at points 3 and 4 (section f-g, Fig. 17). The stage lasts for about 280 days. Finally, in the *Post transitional stage* even the further parts of bentonite hydrate with liquid water, see Fig. 17 g-h. By this time all the observed points show a gradual decrease in suction values.

3.2.2. Mock-up Test: Thermal coupling analyses

Figs. 18-22 show the results of the simulations of Mock-up tests with certain thermal couplings removed. We analyse the couplings below, starting with those affecting the results most. Similar to infiltration test, to view the complete set of net mean stress results versus time for all the thermal couplings in Mock-up test, refer to the supplementary data file (MeanStress_MockupTest.avi).

a) *Vapour density thermal coupling concerning reference saturated density* $[T8 - \rho_w^g(\rho_{w0}^g, T)]$ – Neglecting thermal dependency of vapour density again shows the most variation among the trial cases. The maximum increase in the peak value of mean effective stress (Fig. 18) is about 20% when compared to the baseline model at the end of the simulation. It further supports the earlier finding that neglecting thermal dependency of vapour density leads to an overall reduction in the evaporation process, resulting in a greater extent of hydration. It is also evident from lower suction values (vs baseline model) in Fig. 19. a and b. However, unlike the infiltration test, the stresses remain higher throughout the section comparing to the baseline model results, though the variation near the wetting side remains lower than closer to the heating boundary.

A closer inspection of a case with no vapour vs baseline Mock-up test (refer to supplementary data, section S.3) suggests that the overall effect of evaporation and condensation process near the wetting side remains lower than the infiltration test. It is possibly due to the difference in time and test scale of the problem (larger geometry and higher water inlet pressure in Mock-up). Differences in some bentonite properties can also be an additional cause.

b) *Liquid viscosity thermal coupling* $[T10 - \mu_l(T)]$ – In contrast to the infiltration test, the result of a reduction in liquid movement due to

Table 7
Mechanical properties of bentonite, Mock-up test.

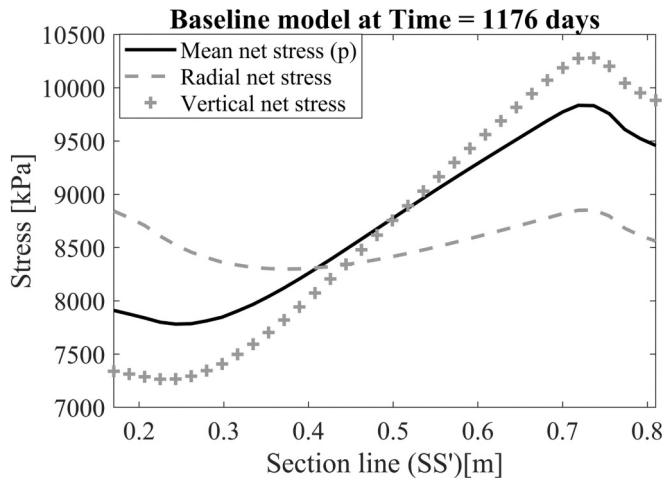| ν	κ_o	κ_{so}	n	α_0 [1/K]	γ_T	α_2	α_k	α_{ks1}	α_{ks2}
0.4	0.05	0.3	0.35	1.5e-4	0.25	0.0	-3.0e-6	0.147	0.0
M	k	p_{ref}^c [kPa]	λ	β [1/kPa]	r	ρ^T	ρ_o^*		
1.0	0.1	12.0	0.15	1e-4	0.925	0.2	1.2e4		

Fig. 16. Mock-up test stresses at $t = 2510$ day along the radial section line SS': mean net stress (swelling pressure) (p), vertical net stress (σ_y), radial net stress (σ_r).

thermally unchanged liquid viscosity (Fig. 20) is evident in the suction figure that shows higher values closer to the heating side (Fig. 19.a and b). The lack of thermal dependency on liquid viscosity thus results in lower bentonite hydration and shows lower mean stress (vs baseline model) in Fig. 18, with a peak difference of about 8% at 2510 days. As a lack of liquid viscosity reduction leads to a lower bentonite permeability for liquid, the results suggest that the transport of water in the liquid phase in the Mock-up test plays a bigger role than in the infiltration test.

c) *van Genuchten temperature coupling [T4 - Van G.(T)]* – Similar to the infiltration test, an isothermal van Genuchten water retention curve shows a higher discrepancy in mean stress result from the baseline case closer to the beginning of the experiment, with the peak difference being approximately 35% at day 19 (see, Fig. 18). The difference gradually reduces to about 7% at the end of the simulation. However, interesting to note here is the variation pattern, at a time over 245 days, depending on the time the trial case shows the peak discrepancy (lower at early-stage vs higher at later) at different locations (near to the wetting side or heating side). Comparing the retention curves between the baseline model and the trial case, it is evident from Fig. 21 that such variations in mean stresses are analogues to retention curve behaviour. Similar to suction, the variations in mean stress remains predominantly high at the early stage (Fig. 19.b and c) and significantly reduces later (Fig. 19.a, b and c).

d) *Thermal coupling due to molecular diffusivity factor [T9 - D_{atm} (T)]* – In this test, the variation in vapour mass flux is low in comparison to the infiltration test. Fig. 22 shows mainly lower vapour flux values near the heating side due to lower molecular diffusivity. Although similar

Fig. 17. Suction evolution during the Mock-up test.

to infiltration test, the thermal uncoupling in this case again causes a gradual increase in suction gradient, as evident from lower suction values at point 1 (vs baseline model, Fig. 19.a) and a relatively similar profile at point 2 (Fig. 19.b). However, here the difference may not be enough to overpower the influence of reduction in molecular diffusivity on vapour flux flow (see, eq. 5 and 26). Furthermore, due to the resulting low suction values (Fig. 19), some variation (higher) in mean effective (Fig. 18) is also evident near the heating side in comparison to the baseline model. The figure shows a peak difference of about 7% at $t = 39$ days, which reduces below 1% at the end of the simulation.

e) *Thermal expansion of water [T5 -β_{wT}]* – Similar to the infiltration test, the thermal expansion of water affects the mean stress (Fig. 18) significantly. Although, unlike the infiltration test, the reduction in mean stress is higher in the early stages of simulation (6.5%, 2% and 3.5% at $t = 19$, 820 and 2510 days, respectively). However, the absolute value of the difference is low early on (10 kPa), while it increases significantly at the end of the simulation to 350 kPa.

The large early-stage discrepancy here in contrast to the infiltration case may also be due to a higher degree of saturation profiles in this case. Fig. 13 and Fig. 21 show that the minimum saturation values are 65% in the case of Mock-up at t = 19 days, whereas it is 45% at t = 20 days in the case of the infiltration test, respectively. The result supports the earlier observation that the lack of this coupling may cause higher suction (see, Fig. 19) and higher flux movements (Fig. 20 and Fig. 22) in the bentonite.

f) *Thermal coupling in relative humidity and suction equilibrium condition [T7 - ρ_w^g(RH$_\psi$, T)]* – As evident from Fig. 22, the trial case again shows a lower vapour mass flux movement due to the uncoupling of temperature in relative humidity and suction equilibrium condition (vs baseline model case). However, in contrast to the previous (infiltration) test case, the influence of the vapour process on mean net stress results (Fig. 18) closer to the wetting side is low. It can be due to the time and test scale of the model and opted parameter values (also noted in RhoV (RhoV0, T) trial case). The simulation shows higher mean stress vs baseline model, specifically closer to the heating side, as evident in Fig. 18 up till 820 days. It is likely because of the greater extent and degree of hydration owning to lower resistance from the vaporization process (see, suction Fig. 19.a). A peak difference in mean stress vs the baseline simulation is about 7% at t = 39 days, reducing to <1% at the end of the simulation.

g) *α_0 [T1]* – Notably, in this test ignoring the elastic volumetric strain rate due to temperature change ($\dot{\varepsilon}_e^T$) also leads to some variation in mean stresses compared to baseline model case (Fig. 18) at the very early stage of the simulation. The stresses reduce to about 5% at t = 19 days. However, as the temperature profiles become stable the difference between this case and the baseline model becomes insignificant. Thus, the effect in this case can be ignored if the emphasis is on long-term bentonite behaviour.

h) *ρ^T [T2], γ_T [T3] and thermal expansions of solids [T6 - β_{sT}]* – Similar to the previous test type, the thermal uncoupling associated with these parameters shows a negligible difference in mean effective stress (Fig. 18) and suction (Fig. 19) profiles (vs baseline model). Thus, these can be neglected. Again, since plastic deformation does not occur, the influence of γ_T cannot be truly determined.

4. Conclusions

The paper examines the influence of ten previously not commonly investigated thermal coupling relationships, representing often-considered physical processes in a THM simulation of a bentonite barrier. The study utilised FE simulations of two experiments, that aimed at replicating certain aspects of deep geological nuclear repository conditions below 100 °C. The analysis of the results suggests that the influence of a given thermal coupling is qualitatively similar in both cases.
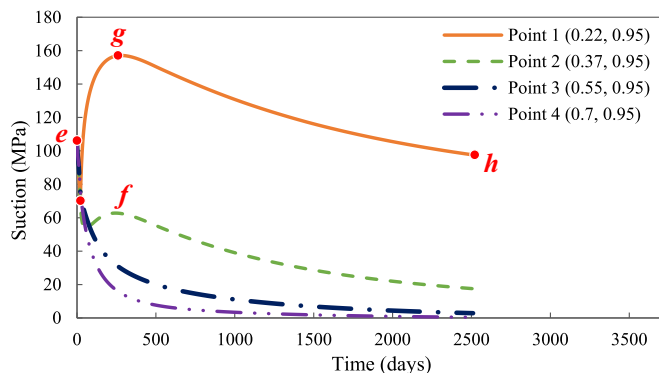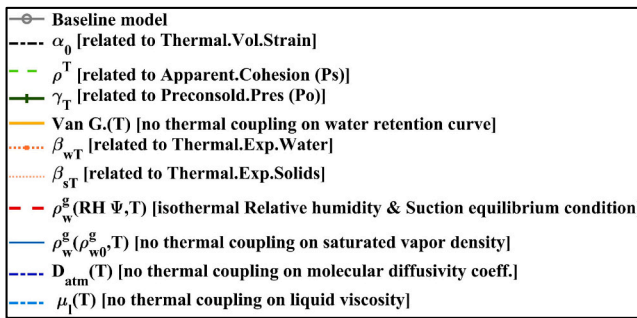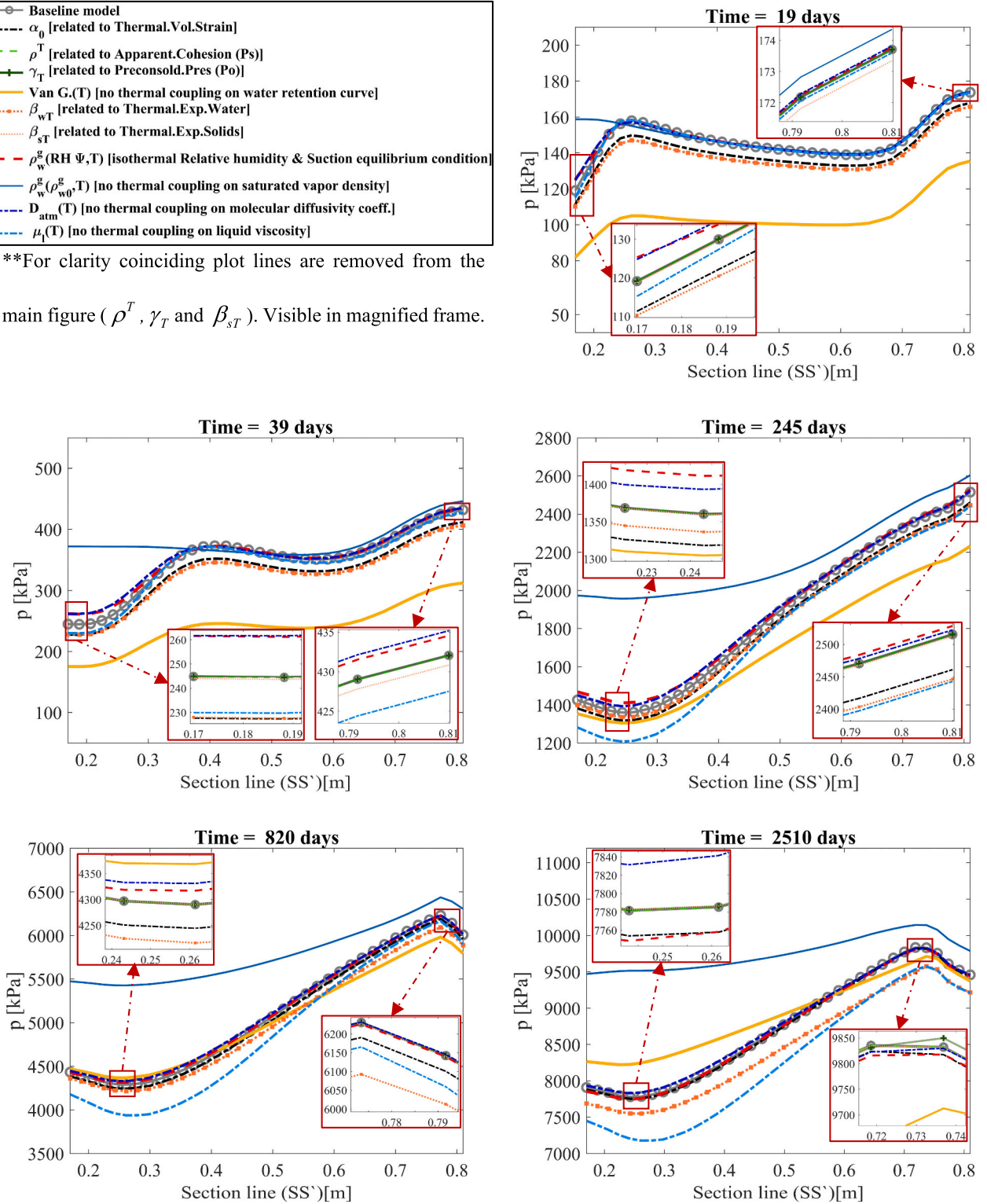
Fig. 18. Mean net stresses (swelling pressure) in Mock-up test, at a radial section line SS'.

However, quantitatively the results vary due to the different time scales, test scales, bentonite properties and boundary conditions. A clear standout from comparing deactivated thermal coupling results with baseline model simulation is the importance of thermal variation in commonly used expression for saturated vapour density (Rocmas code- Rutqvist et al., 1999; OpenGeoSys V6.4.0- Kolditz et al., 2012). Other notable thermally coupled processes affecting the results are associated with vapour and water: fluid viscosity, van Genuchten retention curve,

relative humidity and suction thermal equilibrium condition, molecular diffusivity and thermal expansion of water. On the other hand, thermal couplings associated with soil solids and mechanical constitutive relations such as: ρ^T, α_0, and β_{sT}, show negligible variation in the results. However, the influence of γ_T cannot be evaluated since the soil does not reach plasticity in the simulations. When plastic deformations occur, this factor is likely influential, as indicated by Dupray et al. (2013).

Currently Thebes uses constitutive relationship relatively common in
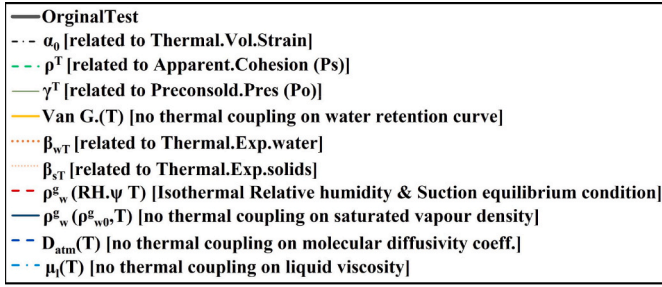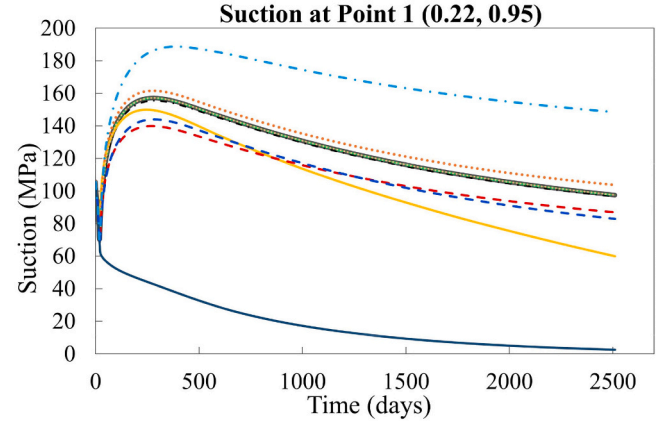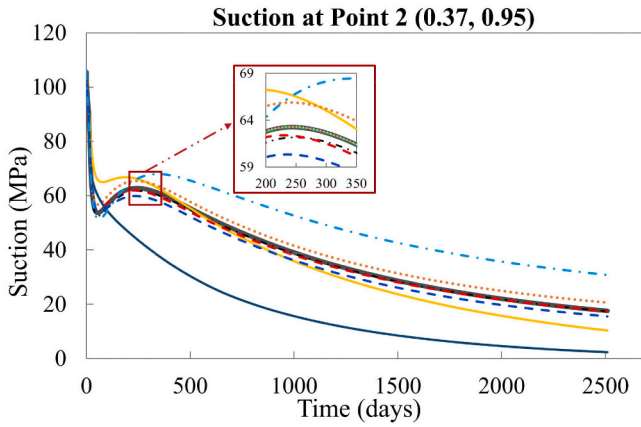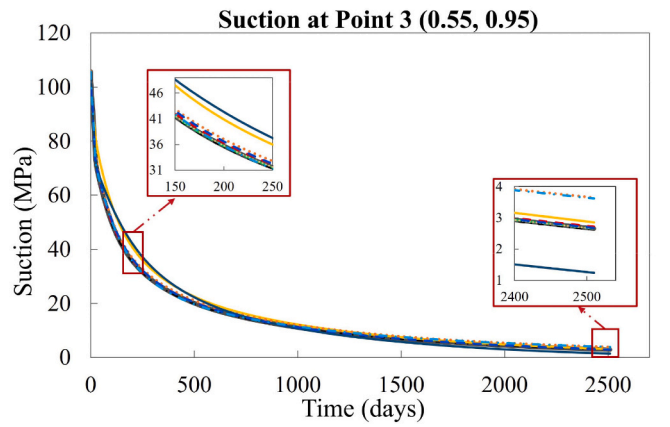
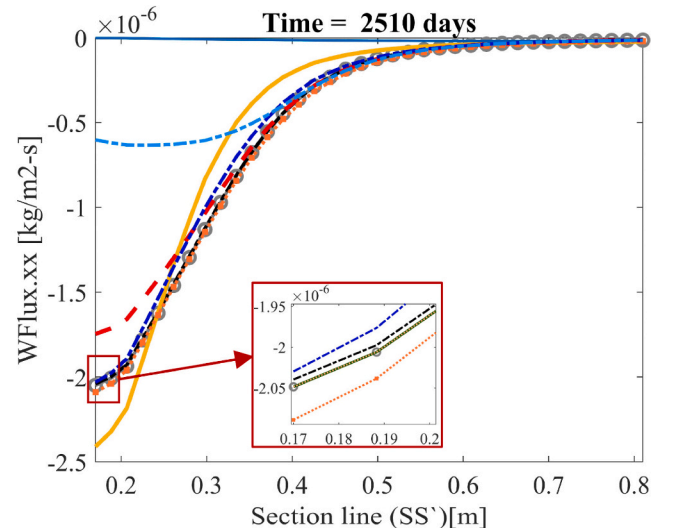**Fig. 19.** Mock-up test, Suction vs time for different cases: a) Point 1, b) Point 2 and, c) Point 3.
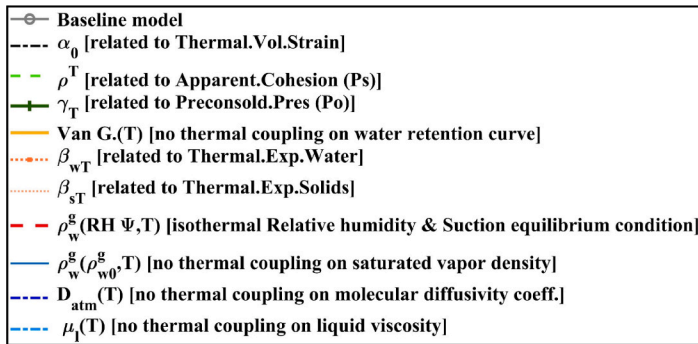
Fig. 20. Mock-up test, water influx in the x-direction along radial section line (SS') (negative sign implies movement towards the left)
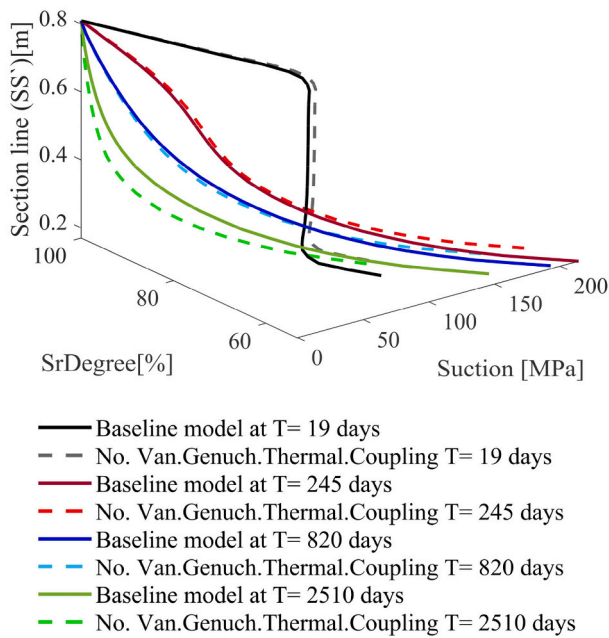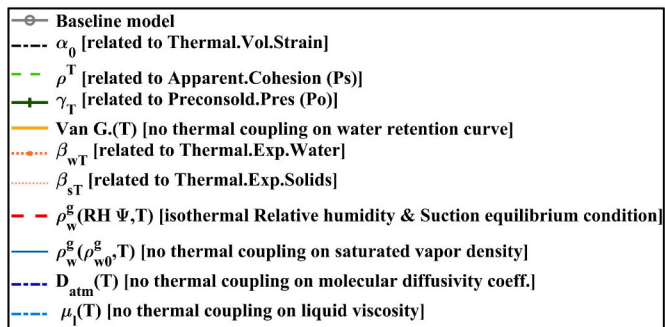
Fig. 21. Mock-up test, water retention along radial section line (SS'): baseline model vs isothermal van Genuchten test case.

the field. In the future, introducing a more accurate version of the identified key coupling equations could be critical in improving the predictive capabilities of numerical simulations. Moreover, the study examines the physical processes that are relevant for THM modelling of bentonite, boom clay or claystone, other research employing different coupled expressions can also utilise the study outcomes to direct development of their models. For example, relations giving thermal variation in saturated vapour density or influence of the temperature on the water retention curve can affect the simulation results significantly. Hence, the accuracy of those relationships and the accuracy of the parameters used for those relationships should be carefully assessed.

A further takeaway from the study is the insights into the dominating physical processes in bentonite when temperature changes replicating geological repository-like conditions. A summary of the key thermal coupling mechanisms, outcomes and underlying physical mechanisms is listed below:

- In both analysed experiments, the change of vapour density with temperature, with respect to its density at reference temperature $\rho_w^g(\rho_{w0}^g, T)$, eq. (27), affects the simulation results most. In the case of the infiltration test, the results show a 155% variation in the mean stress (swelling pressure), whereas in Mock-up it is about 20% difference when compared to the corresponding baseline model simulation at the end of the simulation. Assuming that reference saturated vapour density is not affected by temperature leads to a lack of water vapour transport due to vapour density difference (eq. 6, 24 and 26). It seems that this leads to:
  1) A higher degree of saturation closer to the drying side. The mechanisms occur because of the lower evaporation rate and vapour mass production.
  2) A lower degree of saturation near the wetting side, visible in the case of the infiltration test. This phenomenon is due to lower evaporation in the wetting zone and lower condensation in the heated area of bentonite, leading to lower hydration. It seems that this mechanism may have a lower impact in Mock-up simulation, perhaps due to differences in time scale, soil properties, geometry, and boundary conditions.
- Change of water vapour density with temperature, with respect to the relative humidity and suction thermal equilibrium condtion $\rho_w^g(\mathrm{RH}\_\psi, T)$, eq. (23), shows a similar pattern of outcomes and mechanisms. However, its influence on the mean stress (swelling pressure) is significantly lower than in the previous case. Close to the wetting side, the infiltration test shows a peak difference of 9.5% at t = 20 days which reduces to 1.5% at the end of a simulation. The stresses remain lower near the wetting side at early stages, possibly due to lower vapour evaporation and condensation, whereas at the end of the simulation, mean stresses (swelling pressure) are higher by 8% closer to the drying side due to the increased hydration enabled by lower vapour mass resistance. In the case of Mock-up, the variation in the wetting area is negligible. However, closer to the drying side, the stresses in bentonite are higher by about 7% at t = 39 days.
- Neglecting pore liquid viscosity changes due to temperature [$\mu_l(T)$], eq. (29), appears to be the second most influential factor affecting simulations results. The lack of thermal coupling results in higher suctions and lower water mass influx values in both experiments simulations. That led to lower mean stresses (swelling pressure) in the Mock-up test, with a peak difference of 8%. On the other hand, the infiltration test shows an increase in the mean stress (swelling pressure) value to >250% of the baseline model value near the drying side. We struggle to fully explain such a large discrepancy and we believe it needs further investigation in future.
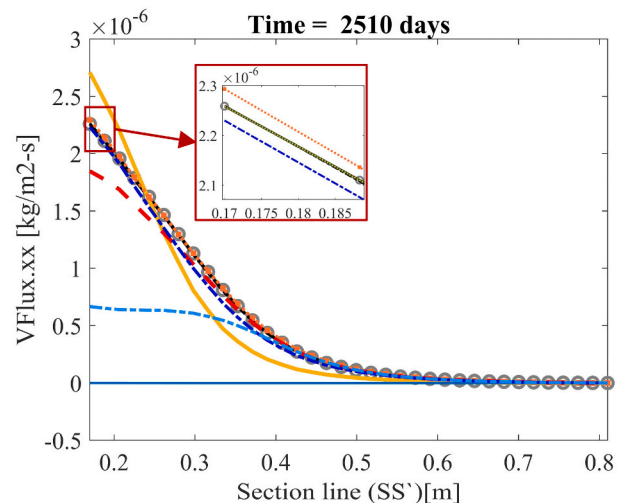

Fig. 22. Mock-up test, vapour mass flux along the radial section line (SS') at 2510 days (positive sign represents a movement towards the right).

- Change in the van Genuchten water retention curve due to temperature change is the third most sensitive coupling affecting the outcomes of the simulations. In the case of the infiltration test, the uncoupling results in a peak difference of about 15% at t = 20 days. This difference eventually reduces to <2% at the end of a simulation. Whereas in Mock-up, these differences are higher, 35% at t = 19 day that reduces to 7% at the end. The variation pattern in stress values seems highly dependent on water retention curve data used in the simulations.

- Switching off the thermal coupling in the molecular diffusivity factor $[D_{atm}(T)]$ in the case of infiltration test leads to higher fluxes near heating and lower at the upper and mid regions. It also leads to higher peak stresses at the drying side by about 21% at $t = 1176$ days and 9% (at t = 20 days) lower peak stresses at the wetting side. These results could be due to a combination of mechanisms: initially lower vapour flux due to lower molecular diffusivity (see, eq. 5, 25, 26, and 28) and, later, higher vapour flux and subsequent condensation due to large suction gradients resulting from lower molecular diffusivity. In the Mock-up test, the latter process seems to be less impactful. Although, noting a higher reduction in suction values near the drying side than in the mid-region, a gradual increase in suction gradient is noticeable. However, the suction change does not lead to higher vapour fluxes. The mean stress (swelling pressure) overall remains lower, with a peak difference of about 7% is observed at t = 39 days.

- Neglecting the thermal expansion of water $[\beta_{wT}]$ leads to a lower mean stress (swelling pressure) value with a peak difference ranging between 6 and 6.5% in the mean stresses in both test cases. Results show lack of such coupling is also linked to higher water flux movements and higher suction in the soil.

- The vapour transport, vapour condensation and vapour evaporation are essential for the results, as further indicated in supplementary data, section S.3.

CRediT authorship contribution statement

Abhishek Gupta: Writing – original draft, Conceptualization, Data curation, Formal analysis, Investigation, Methodology, Software, Validation, Visualization. **Ayman A. Abed:** Formal analysis, Methodology, Software, Supervision, Validation, Writing – review & editing, Conceptualization. **Wojciech T. Solowski:** Conceptualization, Formal analysis, Funding acquisition, Methodology, Supervision, Validation, Writing – review & editing.

Declaration of Competing Interest

The authors declare the following financial interests/personal relationships which may be considered as potential competing interests:

Abhishek Gupta reports financial support was provided by EU Framework Programme for Research and Innovation Euratom. Abhishek Gupta reports financial support was provided by Aalto University.

Supplementary data to this article can be found online at https://doi.org/10.1016/j.enggeo.2023.107251.

Data availability

Data will be made available on request.

Appendix A

The mass conservation of air component [kg/m^3.s] is expressed as:

$$
\left[n\rho_a(H-1)\frac{\partial S^l}{\partial T} + n\rho_a S^l \frac{\partial H}{\partial T} - (1-n)\rho_a\left(S^g + HS^l\right)\beta_{sT} - n\left(S^g + HS^l\right)\frac{M_a}{M_w}\frac{\rho_w^g}{T^2}\left(4974 + g\frac{M_w\psi}{R}\right) \right]\frac{\partial T}{\partial t}
$$

$$
- \left[n\left(S^g + HS^l\right)\frac{M_a}{M_w}\frac{\rho_w^g gM_w}{RT} + n\rho_a(H-1)\frac{\partial S^l}{\partial \psi} - n\rho_a S^l \frac{\partial H}{\partial h_w} \right]\frac{\partial h_w}{\partial t} + \left[n\rho_a(H-1)\frac{\partial S^l}{\partial \psi} \right.
$$

$$
\left. + n\left(S^g + HS^l\right)\left(\frac{M_a \rho_w^l g}{RT} + \frac{M_a}{M_w}\frac{\rho_w^g gM_w}{RT}\right) \right]\frac{\partial h_g}{\partial t} + \rho_a\left(S^g + HS^l\right)\frac{\partial \varepsilon_v}{\partial t} + div(\rho_a q^g) + div(\rho_a H q^l)
$$

$$
- div\left(j_w^g\right) = 0
$$

(A.1)

where ρ_a is the dry air density (assumed same in both liquid and gas phase), H is the Henry's volumetric coefficient of solubility (Vaunat et al., 1997) and M_a is the molar mass of air. Note, due to the limiting condition $\sum_k^m \mathbf{j_k^i} = 0$ (k components and m phases), $-div(\mathbf{j_w^g}) = div(\mathbf{j_a^g})$.

References

Abed, A.A., Sołowski, W.T., 2017. A study on how to couple thermo-hydro-mechanical behaviour of unsaturated soils: physical equations, numerical implementation and examples. Comput. Geotech. 92, 132–155. https://doi.org/10.1016/j.compgeo.2017.07.021.

Abed, A.A., Sołowski, W.T., 2020. Applications of the new thermo-hydro-mechanical-chemical coupled code "Thebes.". Environ Geotech 7, 3–16. https://doi.org/10.1680/jenge.18.00083.

Abed, A.A., Sołowski, W.T., 2021. Estimation of water retention behaviour of bentonite based on mineralogy and mercury intrusion porosimetry tests. Geotechnique 71, 494–508. https://doi.org/10.1680/jgeot.18.P.220.

Alonso, E.E., Gens, A., Josa, A., 1990. A constitutive model for partially saturated soils. Géotechnique 40, 405–430. https://doi.org/10.1680/geot.1990.40.3.405.

Alonso, E.E., Vaunat, J., Gens, A., 1999. Modelling the mechanical behaviour of expansive clays. Eng. Geol. 54, 173–183. https://doi.org/10.1016/S0013-7952(99)00079-4.

Armand, G., Bumbieler, F., Conil, N., et al., 2017. Main outcomes from in situ thermo-hydro-mechanical experiments programme to demonstrate feasibility of radioactive high-level waste disposal in the Callovo-Oxfordian claystone. J. Rock Mech. Geotech. Eng. 9, 415–427. https://doi.org/10.1016/j.jrmge.2017.03.004.

Arson, C., Gatmiri, B., 2008. On Damage Modelling in Unsaturated Clay Rocks, 33, pp. 407–415. https://doi.org/10.1016/j.pce.2008.10.006.

Ballarini, E., Graupner, B., Bauer, S., 2017. Applied Clay Science thermal – hydraulic – mechanical behavior of bentonite and sand-bentonite materials as seal for a nuclear waste repository : Numerical simulation of column experiments. Appl. Clay Sci. 135, 289–299. https://doi.org/10.1016/j.clay.2016.10.007.

Börgesson, L., Chijimatsu, M., Fujita, T., et al., 2001. Thermo-hydro-mechanical characterisation of a bentonite-based buffer material by laboratory tests and numerical back analyses. Int. J. Rock Mech. Min. Sci. 38, 95–104. https://doi.org/10.1016/S1365-1609(00)00067-8.

Chen, Y., Zhou, C., Jing, L., 2009. Modeling coupled THM processes of geological porous media with multiphase flow: theory and validation against laboratory and field scale experiments. Comput. Geotech. 36, 1308–1329. https://doi.org/10.1016/j.compgeo.2009.06.001.

Collin, F., Li, X.L., Radu, J.P., Charlier, R., 2002. Thermo-hydro-mechanical coupling in clay barriers. Eng. Geol. 64, 179–193. https://doi.org/10.1016/S0013-7952(01)00124-7.

Darcy, H., 1856. Les Fontaines Publiques de La Ville de Dijon: exposition et application des principes à suivre et des formules à employer dans les questions de distribution d'eau… un appendice relatif aux fournitures d'eau de plusieurs villes au filtrage des eaux, vol. 1. Dalmont, Paris, France.

De la Morena, G., Navarro, V., Asensio, L., Gallipoli, D., 2021. A water retention model accounting for void ratio changes in double porosity clays. Acta Geotech. 16, 2775–2790. https://doi.org/10.1007/s11440-020-01126-0.

Diersch, H.J.G., Kolditz, O., 2002. Variable-density flow and transport in porous media: Approaches and challenges. Adv. Water Resour. 25, 899–944. https://doi.org/10.1016/S0309-1708(02)00063-5.

Dupray, F., Li, C., Laloui, L., 2013. THM coupling sensitivity analysis in geological nuclear waste storage. Eng. Geol. 163, 113–121. https://doi.org/10.1016/j.enggeo.2013.05.019.

Gens, A., 1995. In: Gens, A., Jouanna, P., Schrefler, B.A. (Eds.), Constitutive Laws BT - Modern Issues in Non-Saturated Soils. Springer Vienna, Vienna, pp. 129–158.

Gens, A., Garcia-Molina, A.J., Olivella, S., et al., 1998. Analysis of a full scale in situ testing simulating repository conditions. Int. J. Numer. Anal. Methods Geomech. 22, 515–548. https://doi.org/10.1002/(SICI)1096-9853(199807)22:7<515::AID-NAG926>3.0.CO;2-8.

Gens, A., Sánchez, M., Guimarães, L.D.N., et al., 2009. A full-scale in situ heating test for high-level nuclear waste disposal: observations, analysis and interpretation. Geotechnique 59, 377–399. https://doi.org/10.1680/geot.2009.59.4.377.

Gens, A., Guimarães, L.N., Olivella, S., Sánchez, M., 2010. Modelling Thermo-Hydro-Mechano-Chemical Interactions for Nuclear Waste Disposal, 2, pp. 97–102. https://doi.org/10.3724/SP.J.1235.2010.00097.

Gens, A., Alcoverro, J., Blaheta, R., et al., 2021. HM and THM interactions in bentonite engineered barriers for nuclear waste disposal. Int. J. Rock Mech. Min. Sci. 137 https://doi.org/10.1016/j.ijrmms.2020.104572.

Guo, G., Fall, M., 2018. Modelling of dilatancy-controlled gas flow in saturated bentonite with double porosity and double effective stress concepts. Eng. Geol. 243, 253–271. https://doi.org/10.1016/j.enggeo.2018.07.002.

Hoffmann, C., Alonso, E.E., Romero, E., 2007. Hydro-mechanical behaviour of bentonite pellet mixtures. Phys. Chem. Earth 32, 832–849. https://doi.org/10.1016/j.pce.2006.04.037.

Jacinto, A.C., Villar, M.V., Gómez-Espina, R., Ledesma, A., 2009. Adaptation of the van Genuchten expression to the effects of temperature and density for compacted bentonites. Appl. Clay Sci. 42, 575–582. https://doi.org/10.1016/j.clay.2008.04.001.

Johnson, L.H., LeNeveu, D.M., Shoesmith, D.W., et al., 1994. Disposal of Canada's Nuclear Fuel Waste: the Vault Model for Postclosure Assessment. At Energy Canada Limited, AECL, pp. 1–404.

Kim, M.J., Lee, S.R., Jeon, J.S., Yoon, S., 2019. Sensitivity analysis of bentonite buffer peak temperature in a high-level waste repository. Ann. Nucl. Energy 123, 190–199. https://doi.org/10.1016/j.anucene.2018.09.020.

Kolditz, O., Bauer, S., Bilke, L., et al., 2012. OpenGeoSys: an open-source initiative for numerical simulation of thermo-hydro-mechanical/chemical (THM/C) processes in porous media. Environ. Earth Sci. 67, 589–599. https://doi.org/10.1007/s12665-012-1546-x.

Lafifi, B., Rouaiguia, A., Boumazza, N., 2019. Optimization of Geotechnical parameters using Taguchi's design of experiment (DOE), RSM and desirability function. Innov Infrastruct Solut 4, 1–12. https://doi.org/10.1007/s41062-019-0218-z.

Laloui, L., Cekerevac, C., 2003. Thermo-plasticity of clays: an isotropic yield mechanism. Comput. Geotech. 30, 649–660. https://doi.org/10.1016/j.compgeo.2003.09.001.

Lee, J.O., Birch, K., Choi, H.J., 2014. Coupled thermal-hydro analysis of unsaturated buffer and backfill in a high-level waste repository. Ann. Nucl. Energy 72, 63–75. https://doi.org/10.1016/j.anucene.2014.04.027.

Liu, H.H., Housewort, J., Rutqvist, J., et al., 2013. Report on THMC Modeling of the near Field Evolution of a Generic Clay Repository : Model Validation and Demonstration. Berkeley, CA, USA, FCRD-UFD-2013–0000244.

Martin, P., Huertas, F.J., National, S., 2006. Large-scale and long-term coupled thermo-hydro-mechanic experiments with bentonite: the FEBEX mock-up test. In: Exp del acoplamiento termo-hidro-mecánico en bentonita a gran escala y larga duración Ens FEBEX en maqueta, 32, pp. 259–282. https://doi.org/10.5209/JIGE.33935.

Mašín, D., 2013. Double structure hydromechanical coupling formalism and a model for unsaturated expansive clays e l, 165, pp. 73–88. https://doi.org/10.1016/j.enggeo.2013.05.026.

Medved, I., Černý, R., 2019. Modeling of radionuclide transport in porous media: a review of recent studies. J. Nucl. Mater. 526 https://doi.org/10.1016/j.jnucmat.2019.151765.

Narkuniene, A., Poskas, P., Kilda, R., Bartkus, G., 2015. Uncertainty and sensitivity analysis of radionuclide migration through the engineered barriers of deep geological repository : case of RBMK-1500 SNF. Reliab. Eng. Syst. Saf. 136, 8–16. https://doi.org/10.1016/j.ress.2014.11.011.

Navarro, V., Asensio, L., Gharbieh, H., et al., 2020. A triple porosity hydro-mechanical model for MX-80 bentonite pellet mixtures. Eng. Geol. 265, 105311 https://doi.org/10.1016/j.enggeo.2019.105311.

Navarro, V., Cabrera, V., De la Morena, G., et al., 2022. A new double-porosity macroscopic model of bentonite free swelling. Eng. Geol. 305, 106725 https://doi.org/10.1016/j.enggeo.2022.106725.

Nguyen-tuan, L., Lahmer, T., Datcheva, M., Schanz, T., 2017. Global and Local Sensitivity Analyses for Coupled Thermo – Hydro – Mechanical Problems, pp. 707–720. https://doi.org/10.1002/nag.2573.

OECD-NEA, 2003. Engineered Barrier Systems and the Safety of Deep Geological Repositories.

Olivella, S., Gens, A., 2000. Vapour transport in low permeability unsaturated soils with capillary effects. Transp. Porous Media 40, 219–241. https://doi.org/10.1023/A:1006749505937.

Önal, M., Sar, Y.Ï., 2007. Thermal behavior of a bentonite. J. Therm. Anal. Calorim. 90, 167–172. https://doi.org/10.1007/s10973-005-7799-9.

Ortiz, L., Volckaert, G., Mallants, D., 2002. Gas generation and Migration in Boom Clay, A Potential Host Rock Formation for Nuclear Waste Storage, 64, pp. 287–296.

Panday, S., Corapcioglu, M.Y., 1989. Reservoir transport equations by compositional approach. Transp. Porous Media 4, 369–393. https://doi.org/10.1007/BF00165780.

Philip, J., De, Vries D., 1957. Moisture movement in porous materials under temperature gradients. EOS Trans. Am. Geophys. Union 38 (2), 222–232. https://doi.org/10.1029/TR038i002p00222.

Potts, D.M., Cui, W., Zdravković, L., 2021. A coupled THM finite element formulation for unsaturated soils and a strategy for its nonlinear solution. Comput. Geotech. 136 https://doi.org/10.1016/j.compgeo.2021.104221.

Rutqvist, J., Noorishad, J., Tsang, C.F., 1999. Coupled Thermohydromechanical Analysis of a Heater Test in Unsaturated Clay and Fractured Rock at Kamaishi Mine. Berkeley, CA, USA, LBNL-44203.

Rutqvist, J., Börgesson, L., Chijimatsu, M., et al., 2001. Thermohydromechanics of partially saturated geological media: Governing equations and formulation of four finite element models. Int. J. Rock Mech. Min. Sci. 38, 105–127. https://doi.org/10.1016/S1365-1609(00)00068-X.

Rutqvist, J., Ijiri, Y., Yamamoto, H., 2011. Implementation of the Barcelona Basic Model into TOUGH-FLAC for simulations of the geomechanical behavior of unsaturated soils. Comput. Geosci. 37, 35–43. https://doi.org/10.1016/j.cageo.2010.10.011.

Rutqvist, J., Zheng, L., Chen, F., 2014. Modeling of Coupled Thermo-Hydro-Mechanical Processes with Links to Geochemistry Associated with Bentonite-Backfilled Repository Tunnels in Clay Formations, pp. 167–186. https://doi.org/10.1007/s00603-013-0375-x.

Sánchez, M.G.A., 2014. Modelling and Interpretation of the FEBEX Mock Up Test and of the Long-Term THM Tests. U Project: Long-Term Performance of Engineered Barrier Systems PEBS: Deliverable D3.3–3. European Commission, Brussels, Belgium.

Sánchez, M., Gens, A., Olivella, S., 2012. THM analysis of a large-scale heating test incorporating material fabric changes. Int. J. Numer. Anal. Methods Geomech. 36, 391–421. https://doi.org/10.1002/nag.1011.

Sánchez, M., Gens, A., Villar, M.V., Olivella, S., 2016. Fully coupled thermo-hydro-mechanical double-porosity formulation for unsaturated soils. Int J Geomech 16, 1–17. https://doi.org/10.1061/(asce)gm.1943-5622.0000728.

Scelsi, G., Abed, A.A., Della, G., et al., 2021. Modelling the Behaviour of Unsaturated Non-Active Clays in Saline Environment, p. 295. https://doi.org/10.1016/j.enggeo.2021.106441.

Schäfers, A., Gens, A., Rodriguez-Dono, A., et al., 2020. Increasing understanding and confidence in THM simulations of Engineered Barrier Systems. Environ Geotech 7, 59–71. https://doi.org/10.1680/jenge.18.00078.

Sellin, P., Leupin, O.X., 2014. The use of clay as an engineered barrier in radioactive-waste management - a review. Clay Clay Miner. 61, 477–498. https://doi.org/10.1346/CCMN.2013.0610601.

SKB, 1999. Waste, repository design and site. In: SKB Tech Rep TR-99-08 (Sotckholm SKB, 1999).

Tran, E.L., Teutsch, N., Klein-BenDavid, O., Weisbrod, N., 2018. Uranium and Cesium sorption to bentonite colloids under carbonate-rich environments: Implications for radionuclide transport. Sci. Total Environ. 643, 260–269. https://doi.org/10.1016/j.scitotenv.2018.06.162.

van Esch, J.M., 2010. Adaptive Multiscale Finite Element Method for Subsurface Flow Simulation. Delft University of Technology, TU Delft.

van Genuchten, M.T., 1980. A Closed-form Equation for predicting the Hydraulic Conductivity of Unsaturated Soils. Soil Sci. Soc. Am. J. 44, 892–898. https://doi.org/10.2136/sssaj1980.03615995004400050002x.

Vaunat, J., Jommi, C., Gens, A., 1997. Statergy for numerical analysis of the transition between saturated and unsaturated flow conditions. In: 6th International Conference on Numerical Models in Geomechanics. Netherlands, pp. 297–302.

Villar, M.V., Gomez-Espina, R., 2009. Report on Thermo-Hydro-Mechanical Laboratory Tests Performed by CIEMAT on Febex Bentonite 2004-2008. Inf Técnicos CIEMAT, p. 1178.

Villar, M.V., Lloret, A., 2004. Temperature influence on the mechanical behaviour of a compacted bentonite. Elsevier Geo-Eng. B Ser 2, 305–310. https://doi.org/10.1016/S1571-9960(04)80058-2.

Villar, M.V., Sánchez, M., Gens, A., 2008. Behaviour of a bentonite barrier in the laboratory: Experimental results up to 8 years and numerical simulation. Phys. Chem. Earth 33, S476–S485. https://doi.org/10.1016/j.pce.2008.10.055.

Villar, M.V., Iglesias, R.J., García-siñeriz, J.L., et al., 2020. Physical evolution of a bentonite buffer during 18 years of heating and hydration. Eng. Geol. 264, 105408 https://doi.org/10.1016/j.enggeo.2019.105408.

Wang, W., Kosakowski, G., Kolditz, O., 2009. A parallel finite element scheme for thermo-hydro-mechanical (THM) coupled problems in porous media. Comput. Geosci. 35, 1631–1641. https://doi.org/10.1016/j.cageo.2008.07.007.

Wang, W., Rutqvist, J., Görke, U.J., et al., 2011. Non-isothermal flow in low permeable porous media: a comparison of Richards' and two-phase flow approaches. Environ. Earth Sci. 62, 1197–1207. https://doi.org/10.1007/s12665-010-0608-1.

Wersin, P., Johnson, L.H., Mckinley, I.G., 2007. Performance of the bentonite barrier at temperatures beyond 100 ° C : a critical review. Phys. Chem. Earth 32 (8–14), 780–788. https://doi.org/10.1016/j.pce.2006.02.051.

Wilson, J., Savage, D., Bond, A., et al., 2011. Bentonite: a review of key properties, processes and issues for consideration in the UK context. Quintessa Rep 1–6. QRS-1378ZG v1 1.

Xu, W.J., Shao, H., Hesser, J., et al., 2013. Coupled multiphase flow and elasto-plastic modelling of in-situ gas injection experiments in saturated claystone (Mont Terri Rock Laboratory). Eng. Geol. 157, 55–68. https://doi.org/10.1016/j.enggeo.2013.02.005.

Ye, W.M., Cui, Y.J., Qian, L.X., Chen, B., 2009. An experimental study of the water transfer through confined compacted GMZ bentonite. Eng. Geol. 108, 169–176. https://doi.org/10.1016/j.enggeo.2009.08.003.

Zheng, L., Samper, J., Montenegro, L., Fernández, A.M., 2010. A coupled THMC model of a heating and hydration laboratory experiment in unsaturated compacted FEBEX bentonite. J. Hydrol. 386, 80–94. https://doi.org/10.1016/j.jhydrol.2010.03.009.

Zheng, L., Rutqvist, J., Xu, H., Birkholzer, J.T., 2017. Coupled THMC models for bentonite in an argillite repository for nuclear waste: Illitization and its effect on swelling stress under high temperature. Eng. Geol. 230, 118–129. https://doi.org/10.1016/j.enggeo.2017.10.002.

Zhou, X., Xu, Y., Sun, D., et al., 2021. Annals of nuclear energy three-dimensional thermal – hydraulic coupled analysis in the nuclear waste repository. Ann. Nucl. Energy 151, 107866. https://doi.org/10.1016/j.anucene.2020.107866.